Morphologies and stellar populations of galaxies in the core of Abell 2218

S. F. Sánchez,[1][*] N. Cardiel,[1,2] M. A. W. Verheijen,[3] S. Pedraz[1,2] and G. Covone[4]

[1]*Centro Astronómico Hispano Alemán, Calar Alto (CSIC-MPI), C/Jesús Durbán Remón 2-2, 04004-Almería, Spain*
[2]*Departamento de Astrofísica, Facultad de Físicas, Universidad Complutense de Madrid, 28040 Madrid, Spain*
[3]*Kapteyn Astronomical Institute, PO Box 800, 9700 AV Groningen, the Netherlands*
[4]*INAF – Osservatorio Astronomico di Capodimonte, Naples, Italy*

ABSTRACT

We present a study of the stellar populations and morphologies of galaxies in the core of the galaxy cluster Abell 2218. Integral field spectroscopy (IFS) observations were performed using PMAS in the PPAK mode covering a field of view of $\sim 74 \times 64$ arcsec^2 centred on the core of the cluster, in order to obtain spectroscopy of an unbiased flux-limited sample of cluster galaxies. 43 objects were detected in the IFS data, 31 of them with enough signal-to-noise ratio to derive the redshift, all of them brighter than $I < 21.5$ mag. 28 are at the redshift of the cluster (17 with previously unknown redshift). Individual spectra of the cluster members were extracted and compared with single stellar population models to derive the luminosity-weighted ages and metallicities. In addition, deep *Hubble Space Telescope* (*HST*)/ACS F475W-, F555W-, F625W- and F850LP-band images centred on the cluster core were obtained from the *HST* archive ($z_{lim} \sim 28$ mag). A detailed morphological analysis of all the galaxies within the field of view of these images down to $z_{lim} < 22.5$ mag was performed classifying them as late-type, intermediate and early-type, on the basis of their Sérsic indices. The literature was scanned to look for spectroscopically confirmed cluster members located within the field of view of the ACS image. The final sample of 59 galaxies comprises our reported sample of 28 galaxies in the core, and 31 additional galaxies in the outer regions. In addition, multiband broad-band photometry was extracted from the literature for all objects.

The morphologically segregated colour–magnitude diagram shows that the early-type galaxies cover the range of brighter and redder colours (the so-called 'red sequence'). A large fraction of spiral galaxies (~ 50 per cent) is found, most of them fainter than the limit of previous studies. They cover a wide range in colours, from blue colours typical of Butcher–Oemler galaxies to red colours similar to those of early-type galaxies. This result indicates that early-type galaxies are more massive and have older stellar populations, while late-type galaxies are less massive and have a wider range of stellar populations. The distribution of luminosity-weighted ages as a function of metallicities and luminosity-weighted masses, and the distribution of Sérsic indices as a function of the luminosity-weighted masses confirm these results. They in fact agree with a proposed two-step scenario for the evolution of galaxies in clusters, where the star formation is quenched first in the infalling spirals, after which a morphological transformation follows that requires larger time-scales. This scenario naturally explains the population faint late-type galaxies with old stellar populations observed in this cluster. In addition, an extremely blue merging galaxy system is found at the core, with the nominal redshift of the cluster.

Key words: techniques: spectroscopic – galaxies: clusters: individual: Abell 2218 – galaxies: elliptical and lenticular, cD – galaxies: fundamental parameters – galaxies: spiral – galaxies: stellar content.

1 INTRODUCTION

Galaxy clusters have been used for decades to study the evolution of galaxies. Being tracers of the largest density enhancements in the Universe, they are considered the regions where galaxies formed

[*]E-mail: sanchez@caha.es

first. At low redshift they are dominated by large early-type galaxies (E/S0), which colours are consistent with a bulk formation of their stars at high redshift. Classically, it was thought that the evolution of this dominant population through different cosmological epochs was largely passive without signatures of important deviations (i.e. periods of more recent star formation). However, this simple picture has changed in the last decades. Butcher, Wells & Oemler (1983) and Butcher & Oemler (1984) showed an increase in the fraction of blue galaxies in clusters with redshift. High-resolution ground-based and *Hubble Space Telescope* (*HST*) images have shown that they correspond to galaxies with late-type morphologies, often disturbed or with close companions (e.g. Thompson 1986; Thompson 1988; Couch et al. 1994; Dressler et al. 1994, 1997). One observes a morphological evolution of the galaxies in clusters, in the sense that the fraction of E-type galaxies remains constant as a function of different cosmological epochs, while the fraction of S0's increases at the expense of L-types towards lower redshift (e.g. Fasano et al. 2000).

The presence in clusters of a significant population of post-starburst galaxies known as 'E + A' or 'k + a' galaxies (Dressler & Gunn 1983; Couch & Sharples 1987), indicates that star formation was active in the recent past and sharply halted at some point during the last 1–1.5 Gyr (Poggianti 2003; Poggianti et al. 2004). Most of these galaxies are late-type, and they show a radial distribution within the clusters that is intermediate between the passive and the emission-line galaxy populations (Poggianti et al. 1999). These results lead to the hypothesis of a two-step evolution of galaxies. A spiral galaxy is captured by the cluster and, during its infall, suffers from gas-stripping due to the tidal forces involved (e.g. Verheijen 1997). Provoked by the lack of gas, the star formation is halted, and the galaxy evolves passively, being observed as a 'k + a' post-starburst. An initial short starburst process, previous to the gas-stripping, may be also present (Poggianti et al. 2004). After this the galaxy evolves morphologically over larger time-scales. The disc dims due to the lack of a new generation of stars, that otherwise will dominate its luminosity, and the galaxy transforms itself into a lenticular galaxy. Dry mergers between lenticular and spheroidal galaxies build up new large spheroidals (e.g. Bell et al. 2006).

The proposed scenario suggests that a fraction of the observed S0's were previously star-forming spirals. For these galaxies the star formation was truncated at some time between 2 and 5 Gyr ago and it is expected that their luminosity faded by ~0.5–1.5 mag and become redder (Poggianti et al. 2001), populating the red sequence at magnitudes fainter than the brightest 1 or 2 mag (Poggianti 2003). The same process may affect dwarf galaxies captured by the cluster, which will suffer more strongly the effects of tidal interaction and galaxy harassment, which induces a short but intense starburst (Moore et al. 1996; Rakos, Dominis & Steindling 2001). Most of the field dwarf galaxies are gas-rich, blue galaxies with late-type morphologies at any redshift (Cairós et al. 2001; Barazza et al. 2006). Once captured by the cluster, consumed or stripped of its gas, it is expected that their luminosity fades and they become redder too, populating the faint-end of the red sequence. In both cases ones expects to find a population of red late-type galaxies, fainter than the original early-type galaxies in the cluster. However, most of the previous studies have found that late-type galaxies are mostly blue (e.g. Thompson 1986).

To test this hypothesis, complete spectroscopic surveys of cluster galaxies and high-resolution deep images for a proper morphological analysis of the faintest possible targets are required. Complete spectroscopic surveys are difficult and time consuming, due to the requirement of deblending and placing objects in the spec-

trograph multislits or masks. In particular, the blending of different components in the core of the clusters is a problem, impossible to handle with classical slit spectroscopy. Due to that, most of the spectroscopic surveys are based on pre-selection of the cluster candidates, most of them based on colour or morphological selections (e.g. Balogh et al. 1999; Dressler et al. 1999; Kelson et al. 2000; Ziegler et al. 2001; Fritz et al. 2005). Alternatively, they are focused on galaxies in the less crowded outer regions. These selections may affect substantially the conclusions. For these reasons we have started an observational programme aimed at obtaining integral field spectroscopy (IFS) of the core of some of the richest galaxy clusters in the local universe, including Abell 1689 (ESO 73.A-0605) and Abell 2218. For both of them deep *HST*/ACS images are available. A similar approach has been used before by Covone et al. (2006), to study the dynamical mass of low redshift galaxy clusters.

Abell 2218 is one of the richest clusters in the Abell catalogue (Abell, Corwin & Olowin 1989), with a richness class of 4. It has a redshift of $z \sim 0.17$, and a velocity dispersion of 1370 km s^{-1} (Kristian, Sandage & Westphal 1978; Le Borgne, Pelló & Sanahuja 1992). The cluster shows a set of arc lenses. Detailed high-resolution X-ray maps (McHardy et al. 1990) and mass-concentration studies based on the properties of the gravitational lenses have shown that the cluster has two density peaks, the strongest of them dominated by a large cD galaxy. Several observational programmes have provided us with a large data set of well-deblended slit spectra for the galaxies in the outer part of the cluster (Ziegler et al. 2001), as well as very good multiband ground-based and *HST* imaging (Le Borgne et al. 1992; Smail et al. 2001; Ziegler et al. 2001). We focused our survey on the central arcmin region of the cluster, around the cD galaxy.

The outline of this article is as follows. Section 2 describes the observational data set, including a description of the IFS data and the *HST*/ACS images. Section 3 includes the analysis of the data set and presents the results. Here, Sections 3.1 and 3.2 describe the automatic morphological analysis that we performed as opposed to classical methods. Section 3.3 shows the method used to deblend and extract the integrated spectra of the different detected objects from the IFS data, with the redshift determination explained in Section 3.4. The analysis of the morphologically segregated colour–magnitude (CM) diagram is included in Section 3.5. The luminosity-weighted ages and metallicities of the galaxies, and their relation to their masses and morphologies are discussed in Section 3.6 and 3.7. The results are discussed in Section 4, and the conclusions are listed in Section 5. Throughout this article we have used a Λ-cosmology, with H$_0$ = 70 km s^{-1} Mpc^{-1}, $\Omega_{\rm m}$ = 0.3 and Ω_{Λ} = 0.7.

2 OBSERVATIONAL DATA SET

2.1 IFS observations and data reduction

Observations were carried out on 2005 June 30 and July 6 at the 3.5-m telescope at Calar Alto Observatory with the Potsdam MultiAperture Spectrograph, PMAS, (Roth et al. 2005) in the PPAK mode (Verheijen et al. 2004; Kelz et al. 2006). The V300 grating was used, covering a wavelength range between 4650–8000 Å with a resolution of ~10 Å full width at half-maximum (FWHM) and a sampling of 3.2 Å pixel^{-1}. The PPAK fibre bundle consists of 382 fibres of 2.7 arcsec diameter each one. Of them, 331 fibres (the science fibres) are concentrated in a single hexagonal bundle covering a field of view of 72 × 64 arcsec^2, with a filling factor of ~65 per cent. The sky is sampled by 36 additional fibres, distributed in six bundles of six fibres each one, located following a circular distribution at ~90 arcsec from the centre and at the edges of the central

hexagon. The sky-fibres are distributed between the science ones in a pseudo-slit, in order to have a good characterization of the sky. The remaining 15 fibres are used for calibration purposes, as described below.

For each night, three dithered exposures of 1 h each were taken, following a pattern of ΔRA $= +1.56$ arcsec and ΔDec. $= \pm 0.78$ arcsec, in order to have a complete coverage of the science field of view and to increase the spatial resolution. Each pointing was divided into shorter individual frames for a proper cosmic ray removal. A total of 6 h integration time was achieved after combining the exposures of the two nights (3 h per night).

Data reduction was performed using R3D (Sánchez & Cardiel 2005; Sánchez 2006), in combination with the IRAF package (Tody 1993)[1] and E3D (Sánchez et al. 2004). The reduction consists of the standard steps for fibre-based integral-field spectroscopy. A master bias frame was created by averaging all the bias frames observed during the night and subtracted from the science frames. The location of the spectra in the CCD was determined using a continuum illuminated exposure taken before the science exposures. Each spectrum was extracted from the science frames by co-adding the flux in 5 pixels in the perpendicular direction of each fibre, and stored in a row-staked-spectrum file RSS (Sánchez et al. 2004). Wavelength calibration was performed using a He lamp exposure taken at the beginning of the night, and corrected for distortions using ThAr exposures obtained simultaneously with the science exposures through the calibration fibres (indicated above). The final accuracy of the wavelength calibration was estimated by comparing the central wavelength of the sky emission lines with their nominal values, finding an agreement within a range of $\sim$0.3 Å. Differences in the fibre-to-fibre transmission throughput were corrected for by comparing the wavelength-calibrated RSS science frames with the corresponding continuum illuminated images. Flux calibration was performed using standard calibration stars observed throughout the night (BD33 + 2642 and Hz44). The uncalibrated spectra of the stars extracted from the reduced frames were then compared with publicly available calibrated spectra, determining a flux calibration correction that was applied to the science frames, once corrected by the differences in exposure time. The accuracy of the spectrophotometric calibration was $\sim$0.15 mag across the wavelength range covered by our data set, as determined by comparing with high accurate broad-band photometry, as we will discuss below. A night-sky emission spectrum was obtained for each pointing by combining the 36 spectra obtained through the sky-fibres, and subtracted from the 331 science-fibre spectra. Fig. 1 shows the average night-sky spectrum obtained after combining all of them. Several strong night-sky emission lines contaminate our spectra, in particular in the reddest part ($\lambda > 7200$ Å).

The three dithered exposures were then combined, creating a single RSS frame with 993 science spectra and the corresponding combination of the position table. A final data cube with 1 arcsec pixel^{-1} sampling was created for each night by interpolating the combined RSS frame using E3D (Sánchez et al. 2004). This corresponds to 2.85 kpc pixel^{-1} at the redshift of our target. Finally, the two data cubes obtained for each night were recentred at each wavelength, correcting for differential atmospheric refraction, and combined using IRAF tasks. The final data cube comprises 4828 individual spectra, covering a field of view of $\sim$71 $\times$ 68 arcsec^2.

---

[1] IRAF is distributed by the National Optical Astronomy Observatories, which are operated by the Association of Universities for Research in Astronomy, Inc., under cooperative agreement with the National Science Foundation.
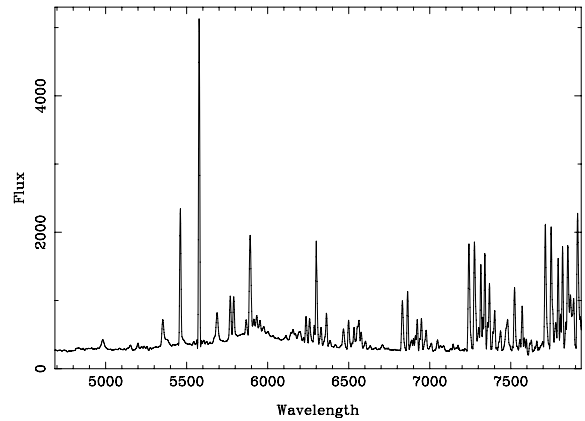
Figure 1. Average night-sky emission spectrum derived by combining the spectra obtained through the 36 sky-fibres for the different pointings of each night.

2.2 *HST*/ACS images and literature data

We obtained publicly available *HST*/ACS images of the cluster in the F475W, F555W, F625W, F775W and F850LP bands from the *HST* archive. Table 1 summarizes their main characteristics, including the central wavelength and width of their bands (obtained from Sirianni et al. 2005). They basically correspond to images in the classical *B*, *V*, *R*, *I* and *z* bands. The images were calibrated to the Vega system using the corresponding magnitude zero-points and prescriptions listed in Sirianni et al. (2005). Table 1 also lists the number of individual frames acquired, each one with a different orientation and a slightly different pointing, due to the observing strategy of the *HST*/ACS camera (in order to cover the gap in between the two different CCDs). The acquired frames were already processed by the *HST*/ACS reduction pipeline, which includes bias and dark current correction, flat-fielding, quantum efficiency correction, field-distortion correction, the derivation of the astrometric solution and flux calibration. We correct each individual from for cosmic rays, realigned to the standard north-east and finally combined into a single image per filter after a sky-background determination and subtraction. The final exposure time and limiting magnitude of each image, estimated by looking for the faintest object detected at $\sim$15σ over the background, are listed in Table 1. All the images are much deeper than our IFS data, as we will see below in detail. In particular this is the case for the F850LP-band image. This image is much deeper than the rest, being as deep as the corresponding image of UDF (e.g. Coe et al. 2006), and therefore one of the deepest images ever taken of this cluster. The cluster core is centred on one of the ACS chips for this particular image, and the field of view of our IFS data is completely covered by it. This high-resolution ACS F850LP-band image will be used for a detailed morphological analysis.

Table 1. Summary of the *HST*/ACS images.

Filter	Pivot λ (Å)	Width (Å)	Number of frames	Exposure time (s)	mag$_{lim}$ (15σ)
F475W	4744.356	418.80	3	4267.0	27.42
F555W	5359.547	375.19	4	5601.0	28.04
F625W	6310.454	415.31	5	7013.0	28.08
F775W	7693.026	432.03	8	10 732.0	27.46
F850LP	9054.768	538.95	12	11 776.0	28.22

We also collected broad-band photometry and redshift information of the cluster galaxies available in the literature. Le Borgne et al. (1992) performed a photometric and spectroscopic survey of the galaxies in a field of 4×4 arcmin^2 centred on Abell 2218. This survey comprises broad-band photometry in five bands (B, g, r, i and z filters) for 729 objects, and redshift determination for 66 of them, 51 cluster members. They calibrated their photometric data using two different systems, the Johnson one for the B band (Johnson & Morgan 1953), and the Thuan–Gunn for the g, r, i and z bands (Thuan & Gunn 1976). We did not perform any recalibration of their data to a common photometric system. These data were initially used to compare with the corresponding intensity of the individual spectra of the objects detected in our IFU data, and for doing so we just needed to use the corresponding Johnson and Thuan–Gunn effective flux (e.g. Fukugita, Shimasaku & Ichikawa 1995). The accuracy of their photometry ranges from 0.1 to 0.5 mag from the brighter ($B \sim 20$ mag) to the fainter ($B \sim 26$ mag) objects. The spectroscopic data lack the required quality needed to perform an accurate analysis of the age–metallicity indicators, like the equivalent widths of Hβ and Mgb, but they provide high quality redshift determinations.

Ziegler et al. (2001) reported on multislit moderate-resolution spectroscopic observations of 48 colour-selected early-type members of the cluster. They also present high-quality multiband photometry in four bands (U, B, V and I), derived from groud-based observations, and a morphological analysis of 19 of the 48 galaxies based on *HST*/WFPC2 observations (F702W band, $\sim R$ band). Finally, Smail et al. (2001) present a photometric study of the ages and metallicities of 81 early-type cluster candidates (33 with confirmed redshifts), based on ground-based K-band and *HST*/WFPC multiband images, in the F450W, F606W and F814W bands. In both cases, their photometric data were calibrated in the Vega-based system. Many other studies have targeted this cluster since its redshift confirmation by Kristian et al. (1978), and the early photometric studies by Butcher et al. (1983). However, in this paper we only use the photometric and spectroscopic data of the articles listed above.
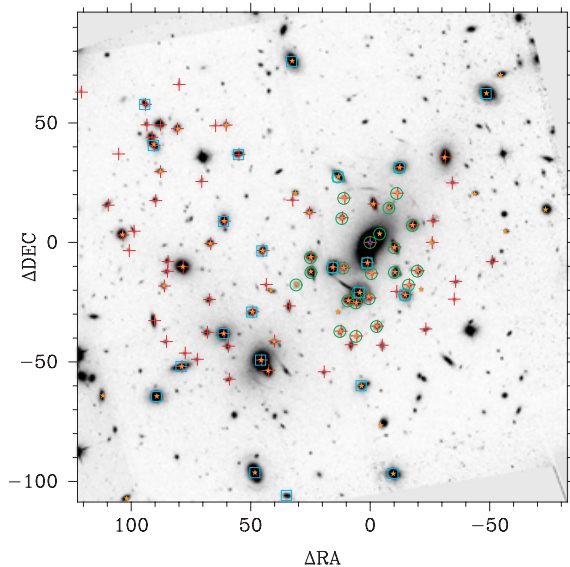

Figure 2. Grey-scale image of the combined F850LP-band image, together with labels indicating the location of the galaxies studied by Le Borgne et al. (1992) (orange stars), Ziegler et al. (2001) (blue squares) and Smail et al. (2001) (red crosses). The location of the confirmed cluster members sampled by our IFS data are also indicated (green circles). North is up and east is towards left-hand side.

Fig. 2 shows a grey-scale of the combined *HST*/ACS F850LP-band image, together with labels indicating the location of the galaxies studied by Le Borgne et al. (1992) (orange stars), Ziegler et al. (2001) (blue squares) and Smail et al. (2001) (red crosses). The location of the confirmed cluster members sampled by our IFS data are also indicated (green circles). As we will see below, most of them have not been previously targeted by any spectroscopic survey.

2.3 The depth of our IFS data

To obtain a rough estimate of the depth of our IFS data, we compared them with available deep optical images. Fig. 3 shows a three-colour image created by co-adding the flux of the final data cube through three broad-bands corresponding approximately to B, R and I (left-hand panel), together with a similar image created using the previously described *HST*/ACS data set. It is interesting to note the similarities between the two images, despite the fact that our data cube has a final FWHM for point-like sources of ~ 2.5 arcsec, much larger than the one from the ACS. Based on the I-band magnitude of the faintest detected object, we roughly estimate the detection limit for our IFS data $I_{lim} \sim 22.4$ mag. However, we only get high enough quality spectra for the proposed study for objects brighter than $I < 21.5$ mag (signal-to-noise ratio $> 5\sigma$ per spectral pixel), as we will see below. This limit is far beyond previous spectroscopic studies on this cluster, around $I_{lim} \sim 18.7$ mag (Ziegler et al. 2001).

3 ANALYSIS AND RESULTS

3.1 Photometric analysis

We used the previously described *HST*/ACS images to obtain homogeneous multiband photometry for all the detected objects in field of Abell 2218. This homogeneous photometric data set is fundamental to estimate the accuracy of the spectrophotometric calibration of our IFS data and to study the stellar populations of the galaxies in the cluster. We use SExtractor (Bertin & Arnouts 1996) to detect objects in the images up to 15σ over the sky (20 connected pixels with a signal-to-noise ratio of at least 2σ each one). This limit is very relaxed, and most probably we are losing many real faint objects by using it. However, we are not interested in the faintest targets, most probably high-z objects or arc lenses (see Fig. 1), but only in the cluster members. For each detected target we obtained aperture photometry in each band, using the MAG_BEST parameter derived by SExtractor. The little variations of the *HST*/ACS point spread function (PSF) compared to the size of our targets of interest guarantees homogeneous photometric data set. Table 2 lists the results from this analysis for the 59 galaxies confirmed to be cluster members, using the published data listed above or the results from our spectroscopic survey (see below). For each target it includes the SExtractor ID, the coordinates (RA and Dec.), and the photometry in each band plus errors. Due to the change of orientation and slightly different pointing of the individual *HST*/ACS frames, the F850LP band covers a slightly larger area than the images in the other bands, and some of the objects were only detected in this band.

3.2 Morphological analysis

One of the goals of the present study is to determine the stellar populations of galaxies in the cluster as a function of their morphologies, in order to understand their origin and evolution. To achieve this goal we performed a morphological analysis of the *HST*/ACS F850LP
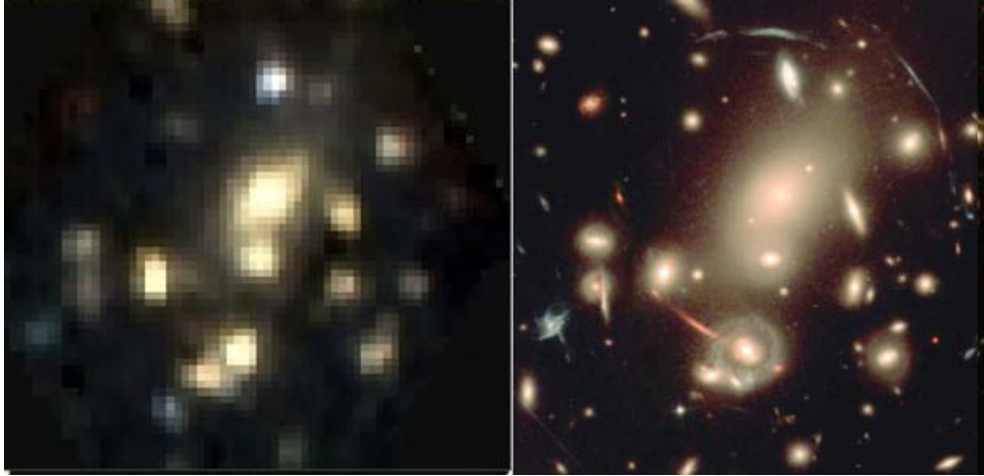
Figure 3. Left-hand panel: three-colour image created by co-adding the flux of the final data cube through three broad-bands corresponding approximately to *B*, *R* and *I*. Right-hand panel: similar image created using *HST*/ACS data described in the text. An electronic version of the full size image can be found in the webpage http://www.caha.es/sanchez/abell2218/BRI_big.jpg.

images, the deepest of our data set, following the prescriptions presented in Coe et al. (2006), where similar images were analysed. This analysis recovers, for each galaxy, the Sérsic index, the integrated magnitude, the effective radius, the ellipticity, the position angle and the asymmetry index.

For undisturbed galaxies the Sérsic index *n* correlates fairly well with morphological type (e.g. Andredakis, Peletier & Balcells 1995; Bell et al. 2004), in the sense that galaxies with high *n* have higher central concentrations (i.e. bulge dominated galaxies) than galaxies with low *n* (i.e. disc dominated galaxies). Less well behaved galaxies, including mergers and irregulars, generally do not have well defined Sérsic indices. Fortunately, these galaxies can generally be weeded out (or selected for) by measuring their large asymmetries (e.g. Conselice et al. 2003).

In summary the morphological analysis consists of the following steps. First, we use SExtractor (Bertin & Arnouts 1996) to detect galaxies in the combined F850LP-band image. For each detected galaxy we recover the physical and image coordinates (RA, Dec., *X* and *Y*), the integrated magnitude (mag_best), the scalelength (r_{50}), the position angle and the ellipticity. Then, we create a postage stamp $5 \times r_{50}$ on a side, for the brightest galaxy. Within that postage stamp, neighbouring galaxies are masked out using ellipses, each ellipse given a minor axis length $b = 2 \times r_{50}$ for that galaxy. Using GALFIT (Peng et al. 2002), the brightest galaxy is fitted to a single component Sérsic model $\Sigma(R) = \Sigma_e \times \exp\{-\kappa_n [(R/R_e)^{1/n} - 1]\}$, where R_e is the effective or half-light radius, Σ_e is the effective surface density, $\Sigma(R)$ is the surface density as a function of radius and $\kappa = \kappa(n)$ is a normalization constant. The fit is constrained to $0.2 < n < 8$ and $0.3 < R_e < 500$ pixels, and the centroid is confined to within 2 pixels of the position derived by SExtractor. As initial guesses for the GALFIT parameters, we use the SExtractor output parameters. Lacking estimates for the Sérsic index from SExtractor, we start all fits with $n = 1.5$. GALFIT convolves the model with the required PSF. Prior to the fit, we created a PSF image by combining postage stamps of unsaturated point-like objects extracted from the combined F850LP-band image.

Having been calculated for the brightest galaxy, the Sérsic model is subtracted from the F850LP-band image. This subtraction benefits the subsequent modelling of fainter nearby galaxies. We then proceed to model the second brightest galaxy, and continue in order of decreasing brightness, modelling and subtracting every galaxy in the SExtractor catalogue. GALFIT is able of simultaneous fit several targets, producing reasonable results, in most of the cases. However, in this case the fitting process is dominated by the brighter targets, and flux of the fainter ones is more poorly recovered. We performed extensive tests before adopting the described procedure. In addition, we determine the asymmetry index (*A*), following the prescriptions in Coe et al. (2006). Of the 802 objects detected by SExtractor in the F850LP-band image brighter than $z < 26.5$ mag, we applied GALFIT to the 241 galaxies brighter than $z < 22.5$ mag. The error in the derived Sérsic index is restricted to a range of ± 0.25, based on the simulations presented in Coe et al. (2006), and therefore a morphological segregation based on that parameter is reliable. The remaining galaxies are far beyond the depth of our spectroscopic data, and therefore excluded. Table 3 lists the resulting fitted parameters and their uncertainties for the 59 galaxies confirmed to be cluster members, using the published data listed above or the results from our spectroscopic survey (see below). It includes, for each galaxy, the SExtractor identification, the χ^2/ν of the fitting procedure, the *z*-band magnitude, the effective radius (R_e), the axis ratio (*a/b*), the position angle (θ), the Sérsic index (n_s) and the asymmetry index (*A*). The listed errors were estimated based on the results of the simulations presented in Coe et al. (2006). The error in the asymmetry index is difficult to quantify for individual objects, however, based on the quoted simulations, we estimate it to be lower than ∼0.1 for the galaxies of our sample. Of all these galaxies, only one has a strong asymmetry index (∼0.8). This galaxy is covered by the field of view of our IFS data, and it will be discussed later in detail.

3.3 The Sérsic indices and the Hubble sequence

Our morphological classification scheme is based on the Sérsic index of the galaxy profile. We consider this automatic classification scheme more straightforward, easy to reproduce, and less subjective than the classical *by-eye* classification (read Wolf et al. 2005, for an illustration of the problem). However, most of the previous studies on the morphologies of galaxies in clusters are based on *by-eye* classifications following the Hubble scheme (Hubble 1926), revised by de Vaucouleurs, de Vaucouleurs & Corwin (1976). Normally, they

Table 2. Summary of the photometric analysis.

ID	RA	Dec.	B_{475}	V_{555}	R_{625}	I_{775}	z_{850}
1	248.953 7297	+66.211 7906	18.09 ± 0.02	17.29 ± 0.02	16.52 ± 0.01	15.85 ± 0.01	15.44 ± 0.01
247	248.985 3560	+66.198 1066	18.73 ± 0.03	17.94 ± 0.02	17.14 ± 0.02	16.44 ± 0.01	16.08 ± 0.02
169	248.987 0850	+66.185 0276	18.86 ± 0.03	18.09 ± 0.03	17.34 ± 0.02	16.70 ± 0.02	16.19 ± 0.02
512	248.956 9254	+66.205 9389	18.92 ± 0.03	18.32 ± 0.03	17.51 ± 0.02	16.80 ± 0.02	16.44 ± 0.02
554	248.954 6845	+66.209 4133	19.53 ± 0.04	18.87 ± 0.04	18.26 ± 0.03	17.56 ± 0.03	17.00 ± 0.03
172	249.007 8962	+66.208 9431	19.22 ± 0.04	18.46 ± 0.03	17.67 ± 0.02	16.96 ± 0.02	16.47 ± 0.02
501	248.964 6342	+66.208 8796	19.40 ± 0.04	18.67 ± 0.04	17.93 ± 0.03	17.12 ± 0.02	16.61 ± 0.03
561	248.976 2849	+66.232 8158	19.33 ± 0.04	18.62 ± 0.04	17.92 ± 0.02	17.17 ± 0.02	16.65 ± 0.03
189	248.996 1745	+66.201 1969	19.57 ± 0.05	18.75 ± 0.04	17.93 ± 0.02	17.27 ± 0.02	16.78 ± 0.03
103	249.015 4109	+66.193 9177	19.50 ± 0.05	18.72 ± 0.04	17.91 ± 0.02	17.25 ± 0.02	16.68 ± 0.03
132	249.008 2842	+66.197 3755	19.57 ± 0.05	18.76 ± 0.04	17.95 ± 0.03	17.27 ± 0.02	16.73 ± 0.03
555	248.946 8602	+66.211 1799	19.92 ± 0.05	19.19 ± 0.05	18.44 ± 0.03	17.69 ± 0.03	17.14 ± 0.03
201	249.016 2635	+66.223 0941	19.61 ± 0.05	18.83 ± 0.04	18.09 ± 0.03	17.39 ± 0.02	16.89 ± 0.03
2	248.945 3711	+66.220 4800	19.89 ± 0.06	19.10 ± 0.05	18.35 ± 0.03	17.65 ± 0.03	17.12 ± 0.03
256	248.983 3226	+66.196 8621	19.89 ± 0.05	19.20 ± 0.05	18.46 ± 0.03	17.80 ± 0.03	17.20 ± 0.04
509	248.960 2122	+66.205 0146	20.20 ± 0.06	19.44 ± 0.05	18.43 ± 0.03	17.73 ± 0.03	17.26 ± 0.04
349	248.995 9951	+66.214 2513	20.00 ± 0.06	19.23 ± 0.05	18.54 ± 0.03	17.77 ± 0.03	17.27 ± 0.04
126	249.025 3609	+66.212 6854	19.90 ± 0.06	19.12 ± 0.05	18.41 ± 0.03	17.73 ± 0.03	17.26 ± 0.04
570	248.963 0196	+66.219 4216	20.11 ± 0.06	19.35 ± 0.05	18.62 ± 0.04	17.93 ± 0.03	17.41 ± 0.04
523	248.987 1643	+66.238 7374	–	–	–	–	17.39 ± 0.04
604	248.952 8976	+66.216 2360	19.41 ± 0.04	18.95 ± 0.04	18.35 ± 0.03	17.94 ± 0.03	17.49 ± 0.04
599	248.943 7771	+66.205 6763	20.23 ± 0.07	19.40 ± 0.05	18.65 ± 0.04	18.00 ± 0.03	17.46 ± 0.04
658	248.941 5886	+66.213 7478	20.29 ± 0.07	19.53 ± 0.06	18.80 ± 0.04	18.11 ± 0.04	17.59 ± 0.04
337	248.987 8980	+66.203 7120	20.53 ± 0.08	19.76 ± 0.06	18.97 ± 0.04	18.35 ± 0.04	17.64 ± 0.05
596	248.946 8067	+66.208 3220	20.68 ± 0.08	19.83 ± 0.07	19.07 ± 0.05	18.37 ± 0.04	17.77 ± 0.05
462	248.970 9853	+66.210 0529	20.30 ± 0.07	19.49 ± 0.06	18.85 ± 0.04	18.21 ± 0.04	17.86 ± 0.05
471	248.956 4109	+66.195 1060	20.64 ± 0.08	19.83 ± 0.07	19.03 ± 0.04	18.46 ± 0.04	17.86 ± 0.05
302	248.999 9910	+66.211 6528	20.68 ± 0.08	19.91 ± 0.07	19.18 ± 0.05	18.53 ± 0.04	17.79 ± 0.05
388	248.984 9322	+66.210 8143	20.41 ± 0.07	19.74 ± 0.06	19.08 ± 0.05	18.48 ± 0.04	17.97 ± 0.05
449	248.970 8088	+66.208 2924	20.62 ± 0.56	19.85 ± 0.10	19.05 ± 0.04	18.39 ± 0.04	18.01 ± 0.05
72	249.030 9189	+66.193 9739	–	–	–	–	17.89 ± 0.05
408	248.991 6711	+66.222 0150	20.62 ± 0.08	19.91 ± 0.07	19.19 ± 0.05	–	17.95 ± 0.05
95	249.038 9514	+66.215 5899	20.96 ± 0.09	20.24 ± 0.08	19.53 ± 0.06	18.87 ± 0.05	18.33 ± 0.06
798	249.024 0772	+66.182 0752	–	–	–	–	18.41 ± 0.07
511	248.957 9508	+66.204 7618	20.35 ± 0.11	19.72 ± 0.10	19.25 ± 0.06	18.68 ± 0.06	18.51 ± 0.07
493	248.975 4372	+66.217 4786	21.44 ± 0.12	20.74 ± 0.10	19.99 ± 0.07	19.33 ± 0.07	18.64 ± 0.07
643	248.940 1830	+66.208 4529	21.45 ± 0.12	20.67 ± 0.10	19.97 ± 0.07	19.29 ± 0.06	18.59 ± 0.07
329	249.009 3949	+66.225 0084	21.19 ± 0.11	20.49 ± 0.09	19.69 ± 0.06	19.00 ± 0.06	18.52 ± 0.07
549	248.951 9752	+66.202 0070	21.33 ± 0.11	20.65 ± 0.10	19.94 ± 0.07	19.23 ± 0.06	18.76 ± 0.08
632	248.948 4012	+66.215 7872	21.47 ± 0.14	20.50 ± 0.10	19.84 ± 0.06	19.21 ± 0.06	18.89 ± 0.07
357	248.981 7003	+66.200 2660	21.85 ± 0.14	20.54 ± 0.09	19.73 ± 0.06	19.05 ± 0.06	18.53 ± 0.07
560	248.951 0744	+66.212 7998	22.45 ± 0.19	21.81 ± 0.17	21.06 ± 0.12	20.49 ± 0.12	20.00 ± 0.10
196	249.014 3811	+66.220 0223	21.71 ± 0.13	20.99 ± 0.12	20.26 ± 0.08	19.57 ± 0.07	19.01 ± 0.09
384	248.982 4979	+66.206 1905	21.46 ± 0.12	20.83 ± 0.11	20.17 ± 0.08	19.57 ± 0.07	19.09 ± 0.09
411	248.995 4237	+66.225 4124	21.75 ± 0.14	20.99 ± 0.12	20.27 ± 0.08	19.56 ± 0.07	18.91 ± 0.08
603	248.961 9939	+66.214 6043	21.83 ± 0.14	21.10 ± 0.12	20.37 ± 0.09	19.73 ± 0.08	19.13 ± 0.09
533	248.961 5077	+66.208 8133	22.07 ± 0.15	21.39 ± 0.14	20.60 ± 0.10	19.78 ± 0.08	19.30 ± 0.09
619	248.942 7500	+66.206 8096	21.94 ± 0.15	21.21 ± 0.13	20.58 ± 0.09	19.93 ± 0.09	19.30 ± 0.10
484	248.962 4573	+66.201 4471	21.84 ± 0.14	21.24 ± 0.13	20.52 ± 0.09	19.97 ± 0.09	19.50 ± 0.10
153	249.013 3589	+66.206 7467	21.83 ± 0.14	21.16 ± 0.13	20.41 ± 0.09	19.79 ± 0.08	19.24 ± 0.10
513	248.954 0625	+66.205 2672	22.31 ± 0.23	21.58 ± 0.15	20.64 ± 0.18	19.64 ± 0.18	19.04 ± 0.09
507	248.957 8870	+66.200 8693	22.40 ± 0.20	21.68 ± 0.18	21.03 ± 0.12	20.39 ± 0.11	19.84 ± 0.13
431	248.975 2130	+66.206 8778	20.89 ± 0.09	20.60 ± 0.10	20.27 ± 0.08	19.97 ± 0.09	19.78 ± 0.13
659	248.946 0977	+66.217 4923	23.69 ± 0.34	22.91 ± 0.29	22.14 ± 0.20	21.46 ± 0.18	20.81 ± 0.17
575	248.961 3337	+66.216 9292	22.94 ± 0.24	22.05 ± 0.20	21.43 ± 0.15	20.79 ± 0.13	20.36 ± 0.17
574	248.953 4579	+66.208 1824	23.14 ± 0.32	22.48 ± 0.28	21.74 ± 0.16	21.02 ± 0.14	20.47 ± 0.16

subdivide the galaxies in their different Hubble types, or at least in three groups: pure spheroidals (E-type), lenticulars (S0), and spirals (L-type) (e.g. Fasano et al. 2000; Poggianti et al. 2001; Smail et al. 2001; Ziegler et al. 2001). In order to compare with previous results it is necessary to determine to which type our galaxies, based on their Sérsic indices, correspond.

As we indicated above, Andredakis et al. (1995) show that there is a correlation between the Sérsic index and morphological type. However, here we need to determine how these parameters correlate for our data set. For doing so, we follow Fasano et al. (2000) and create a set of simulated galaxies. Their magnitudes, scalelengths, position angles and ellipticities are extracted from the previously

Table 3. Summary of the morphological analysis.

ID	χ^2/ν	z_{850}	R_e (arcsec)	a/b	θ	n_s	A
1	0.017	16.10 ± 0.02	12.06 ± 0.05	0.49 ± 0.01	37 ± 4	1.63 ± 0.06	0.093
247	0.023	16.21 ± 0.02	5.18 ± 0.05	0.85 ± 0.01	51 ± 4	1.88 ± 0.06	0.175
169	0.024	17.07 ± 0.02	1.66 ± 0.06	0.49 ± 0.02	89 ± 4	1.48 ± 0.07	0.043
512	0.033	17.20 ± 0.02	1.51 ± 0.06	0.77 ± 0.02	-37 ± 8	2.03 ± 0.07	0.156
554	0.034	17.37 ± 0.02	0.63 ± 0.06	0.80 ± 0.02	-10 ± 5	1.80 ± 0.07	0.321
172	0.016	16.84 ± 0.02	1.64 ± 0.06	0.82 ± 0.01	-46 ± 9	2.95 ± 0.06	0.056
501	0.026	15.92 ± 0.02	0.81 ± 0.05	0.84 ± 0.01	50 ± 5	2.86 ± 0.05	0.045
561	0.020	17.25 ± 0.02	1.52 ± 0.06	0.69 ± 0.02	-81 ± 12	1.47 ± 0.07	0.081
189	0.019	17.14 ± 0.02	2.69 ± 0.06	0.90 ± 0.02	-59 ± 10	3.93 ± 0.07	0.088
103	0.011	16.93 ± 0.02	1.17 ± 0.05	0.94 ± 0.01	-26 ± 5	2.69 ± 0.06	0.042
132	0.018	17.28 ± 0.02	1.20 ± 0.06	0.46 ± 0.02	-6 ± 5	2.78 ± 0.07	0.058
201	0.027	17.49 ± 0.02	0.89 ± 0.06	0.50 ± 0.02	-61 ± 10	1.91 ± 0.07	0.132
2	0.013	17.43 ± 0.02	0.96 ± 0.06	0.80 ± 0.02	-16 ± 5	2.63 ± 0.07	0.050
256	0.022	17.64 ± 0.02	0.51 ± 0.06	0.85 ± 0.02	75 ± 5	1.74 ± 0.07	0.078
509	0.028	17.46 ± 0.02	1.09 ± 0.06	0.66 ± 0.02	-33 ± 7	3.19 ± 0.07	0.129
349	0.016	17.98 ± 0.02	0.86 ± 0.07	0.70 ± 0.02	71 ± 4	2.23 ± 0.07	0.077
126	0.033	17.44 ± 0.02	0.68 ± 0.06	0.95 ± 0.02	-83 ± 12	2.00 ± 0.07	0.159
570	0.020	18.32 ± 0.03	1.15 ± 0.08	0.37 ± 0.03	-63 ± 10	1.81 ± 0.08	0.054
523	0.018	17.78 ± 0.02	0.70 ± 0.07	0.57 ± 0.02	-88 ± 13	1.74 ± 0.07	0.047
73	0.018	17.90 ± 0.02	0.83 ± 0.07	0.81 ± 0.02	38 ± 5	2.02 ± 0.07	0.077
604	0.021	18.09 ± 0.03	1.13 ± 0.08	0.44 ± 0.03	84 ± 4	0.72 ± 0.08	0.129
599	0.019	17.76 ± 0.02	1.04 ± 0.07	0.91 ± 0.02	20 ± 5	3.94 ± 0.07	0.051
658	0.016	17.87 ± 0.02	1.01 ± 0.07	0.88 ± 0.02	51 ± 6	2.69 ± 0.07	0.081
337	0.015	17.96 ± 0.02	0.59 ± 0.08	0.78 ± 0.02	5 ± 4	2.49 ± 0.07	0.050
596	0.015	18.96 ± 0.03	0.65 ± 0.09	0.64 ± 0.05	58 ± 6	2.13 ± 0.08	0.067
210	0.041	18.19 ± 0.03	0.47 ± 0.08	0.59 ± 0.03	-21 ± 6	2.03 ± 0.08	0.823
462	0.021	18.21 ± 0.03	1.35 ± 0.08	0.84 ± 0.03	-21 ± 7	2.35 ± 0.08	0.102
471	0.015	18.12 ± 0.03	0.97 ± 0.08	0.89 ± 0.03	3 ± 5	2.11 ± 0.08	0.118
302	0.014	18.14 ± 0.03	0.48 ± 0.08	0.93 ± 0.03	5 ± 6	2.01 ± 0.08	0.048
388	0.015	18.25 ± 0.03	0.71 ± 0.08	0.76 ± 0.03	45 ± 5	1.68 ± 0.08	0.065
449	0.021	18.57 ± 0.03	1.60 ± 0.08	0.87 ± 0.04	89 ± 6	1.03 ± 0.08	0.316
72	0.019	18.64 ± 0.03	0.73 ± 0.09	0.44 ± 0.04	72 ± 5	2.13 ± 0.08	0.057
408	0.017	18.59 ± 0.03	0.72 ± 0.08	0.74 ± 0.04	-12 ± 6	1.46 ± 0.08	0.152
95	0.015	18.41 ± 0.03	0.63 ± 0.08	0.85 ± 0.03	80 ± 6	1.45 ± 0.08	0.062
798	0.020	19.02 ± 0.04	0.88 ± 0.10	0.45 ± 0.06	9 ± 5	0.81 ± 0.09	0.068
511	0.029	18.74 ± 0.03	0.57 ± 0.09	0.53 ± 0.04	-67 ± 12	2.35 ± 0.08	0.169
493	0.018	18.99 ± 0.03	0.45 ± 0.09	0.72 ± 0.06	-42 ± 9	1.56 ± 0.08	0.058
643	0.014	19.09 ± 0.04	0.45 ± 0.10	0.99 ± 0.06	84 ± 13	1.74 ± 0.09	0.094
329	0.015	18.71 ± 0.03	0.76 ± 0.09	0.77 ± 0.04	41 ± 6	1.46 ± 0.08	0.071
549	0.012	19.04 ± 0.04	0.63 ± 0.10	0.95 ± 0.06	-35 ± 9	1.77 ± 0.09	0.067
632	0.017	19.03 ± 0.04	0.37 ± 0.10	0.73 ± 0.06	-82 ± 13	1.49 ± 0.09	0.102
357	0.018	18.70 ± 0.03	0.60 ± 0.09	0.67 ± 0.04	-9 ± 6	1.07 ± 0.08	0.184
560	0.049	18.39 ± 0.03	0.17 ± 0.08	0.87 ± 0.03	-74 ± 12	0.53 ± 0.08	0.469
503	0.013	19.33 ± 0.04	0.83 ± 0.10	0.80 ± 0.07	13 ± 6	0.97 ± 0.09	0.133
196	0.016	19.14 ± 0.04	0.51 ± 0.10	0.67 ± 0.06	-8 ± 6	1.38 ± 0.09	0.079
384	0.017	19.53 ± 0.06	0.77 ± 0.12	0.43 ± 0.08	-45 ± 10	1.29 ± 0.09	0.067
411	0.010	18.86 ± 0.03	0.39 ± 0.09	0.96 ± 0.04	-81 ± 13	1.88 ± 0.08	0.080
603	0.012	19.59 ± 0.06	0.49 ± 0.12	0.96 ± 0.08	43 ± 9	1.19 ± 0.09	0.059
533	0.015	18.87 ± 0.03	0.27 ± 0.09	0.94 ± 0.04	65 ± 9	1.44 ± 0.08	0.045
619	0.015	19.55 ± 0.06	0.41 ± 0.12	0.74 ± 0.08	5 ± 6	1.29 ± 0.09	0.069
484	0.017	19.71 ± 0.06	0.75 ± 0.13	0.51 ± 0.08	36 ± 5	1.18 ± 0.09	0.078
153	0.013	19.69 ± 0.06	0.69 ± 0.13	0.72 ± 0.08	-76 ± 13	1.34 ± 0.09	0.062
513	0.024	20.04 ± 0.08	1.15 ± 0.17	0.50 ± 0.10	39 ± 10	2.31 ± 0.10	0.194
507	0.013	20.27 ± 0.09	0.38 ± 0.18	0.85 ± 0.11	74 ± 10	1.31 ± 0.10	0.061
431	0.014	20.20 ± 0.09	1.10 ± 0.18	0.85 ± 0.11	32 ± 11	0.89 ± 0.10	0.218
803	0.017	21.21 ± 0.16	0.67 ± 0.26	0.86 ± 0.15	64 ± 17	0.40 ± 0.15	0.240
659	0.019	20.66 ± 0.11	0.25 ± 0.22	0.81 ± 0.12	-83 ± 17	1.68 ± 0.12	0.085
575	0.010	20.86 ± 0.09	0.75 ± 0.24	0.85 ± 0.12	-40 ± 13	1.39 ± 0.13	0.119
574	0.011	20.49 ± 0.06	0.27 ± 0.22	0.84 ± 0.11	-89 ± 18	1.15 ± 0.12	0.073

described morphological catalogue of 241 galaxies. For each entry in the morphological catalogue 20 galaxies were simulated, each one with a different bulge-to-disc ratio, ranging randomly from 0.01 (almost a pure disc) to 1000 (almost a pure spheroidal). Each galaxy image was created using GALFIT, with a two components Sérsic model, one with $n_s = 4$ for the bulge and another with $n_s = 1$ for the disc, convolving them with the same PSF used in the morphological analysis. Finally, noise was added following the prescription presented in Coe et al. (2006) and Sánchez et al. (2004a) for simulating ACS images, to resemble as much as possible the original F850LP-band image.

The same morphological analysis described in the previous section was performed for each of the simulated galaxy images, fitting them to a single component Sérsic model. Finally, we end up with ∼5000 simulations comprising the recovered Sérsic index for a certain bulge-to-disc ratio. Simien & de Vaucouleurs (1986) show the typical bulge-to-disc ratios for the different families of galaxies in the revised Hubble sequence. In particular, they present the mean fractional luminosity of the spheroidal component of the galaxies and its corresponding magnitude difference for each galaxy type. Fig. 4 shows the Sérsic indices of the simulated galaxies as a function of these magnitude differences (Δ mag). The differences for various families of galaxies along the Hubble sequence are indicated (extracted from Simien & de Vaucouleurs 1986). Based on this figure we adopted the following scheme to morphologically classify galaxies based on the Sérsic indices: galaxies with $n_s > 2.5$ are considered spheroidals (E-type), galaxies with $1.75 < n_s < 2.5$ are considered intermediate type (mostly S0's, but strongly contaminated by other families of bulge-dominated spirals, like Sa and Sb), and galaxies with $n_s < 1.75$ are considered spirals (L-type).

This classification scheme is based on the fair correlation between the bulge-to-total luminosity ratio and the Hubble type of a galaxy Simien & de Vaucouleurs (1986). However, we may admit that some degree of contamination is expected among the different morphological subgroups due to the dispersion in this correlation. Although we can clearly distinguish between pure spheroidals (E-type) and spirals (L-type), the subgroup of intermediate type is most probably less accurately defined, with considerable contami-

nations from both extreme subgroups. Another source of criticism about the adopted scheme is the fact that some dwarf elliptical galaxies shown low Sérsic indices (e.g. Barazza, Binggeli & Jerjen 2003). Although in galaxy surveys without morphological pre-selections most of the galaxies with low Sérsic indices are spiral galaxies Andredakis et al. (1995), the contamination from dwarf ellipticals could be a potential problem in the study of galaxy clusters. To address this problem we perform a visual inspection of the 29 galaxies with $n_s < 1.75$ listed in Table 2 and 3 (i.e. the ones classified as spirals) using the previous described *HST*/ACS images. Only two of these 29 galaxies (∼7 per cent) could be classified as dwarf spheroidals based on this visual inspection. However, both of them are nearby brighter galaxies, and their low surface brightness areas (like disc structures) are not clearly distinguished. In any case, the possible contamination by dwarf spheroidal galaxies is expected to be marginal. The remaining galaxies show clear evidence of disc structures. Taking into account these caveats we consider that the adopted classification scheme is valid within the context of this study.
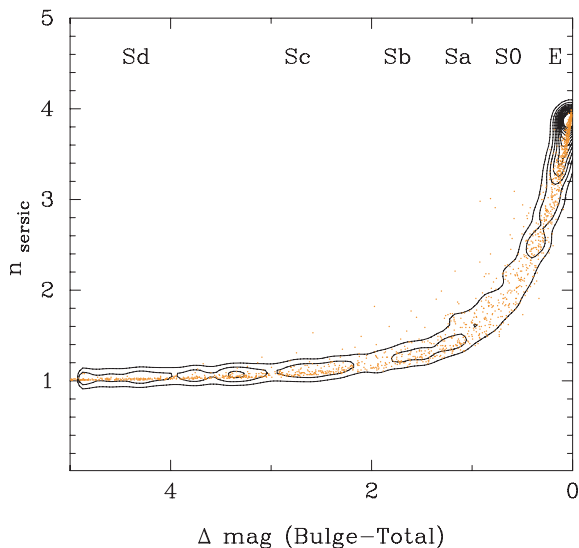
3.4 Spectra extraction

To deblend and extract the integrated spectra of each individual galaxy in the field we used a technique for 3D crowded field spectroscopy developed by ourselves (Sánchez et al. 2004b; García-Lorenzo et al. 2005; Sánchez et al. 2006a). The technique is an extension to IFS of GALFIT (Peng et al. 2002), that we named GALFIT3D. It consists of a deblending of the spectrum of each object in the data cube by fitting of analytical models. IFS data may be understood as a set of adjacent narrow-band images, with the width of the spectral pixel. For each narrow-band image it is possible to apply modelling techniques developed for 2D imaging, like GALFIT, and extract the morphological and flux information for each object in the field at each wavelength. The spectra of all the objects are extracted after repeating the technique through the data cube. We have already shown that the use of additional information to constrain the morphological parameters increases the quality of the recovered spectra (Sánchez et al. 2006a). With that purpose we used the morphological parameters previously derived from the *HST*/ACS F850LP-band image.

We create a 2D image by co-adding the flux through the useful wavelength range (4650–8000 Å) covered by our data cube. After this, we cross-checked by eye this image, looking for those galaxies detected in the F850LP band for which we had performed a morphological analysis. We detect 41 objects (40 galaxies and one star) in the collapsed 2D image, out to $z < 23$ mag. The gravitational arc lenses were excluded since their study is out the scope of the current work. Fig. 5 shows a grey-scale of the co-added 2D image derived from the data cube, together with an identification label at the location of each of the detected objects.

As we mentioned before, we use the previously derived morphological parameters for each galaxy to extract its integrated spectrum by modelling each galaxy in the data cube with GALFIT3D. We use the same model that was used to fit the F850LP-band image, with all the morphological parameters fixed, and fitting only the flux at each wavelength. For each wavelength, we created a PSF using postage stamp images of the only field-star in the field of view of our IFS data. As in the previous morphological analysis, the 3D fit was performed in a sequential way. We first extracted the spectrum of the brightest galaxy, the central cD, masking the neighbouring galaxies. Once extracted, its 3D model was subtracted to the original data cube, and the spectrum of the second brightest galaxy was extracted. The process continued iteratively until the faintest galaxy spectrum was
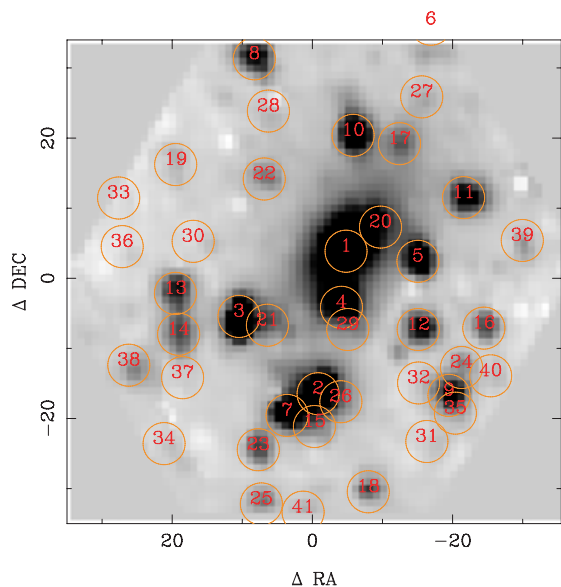

Figure 4. Results from the simulations. Solid dots show the recovered Sérsic indices of the simulated galaxies as a function of the magnitude difference between the bulge and total components (Δmag). Overplotted contours show the density distribution of the plotted points.

Figure 5. Grey-scale representation of the 2D image obtained by co-adding the flux from the data cube through all the covered wavelength range (4650–8000 Å). The circles indicate the location of the detected galaxies in the data cube, together with a number indicating the label code used to identify them.

extracted. The individual spectra are shown in Appendix A. All of them are background limited. Thus, the signal-to-noise ratio can be estimated from the background-noise level. We used the variations in the sky spectrum in each sky-fibre to determine the level of background noise. In this way, we estimated that the signal-to-noise ratio of the extracted spectra range between ∼1000 and ∼5 per spectral pixel for the brightest and faintest targets, respectively. The signal-to-noise ratio is affected strongly by the sky emission lines (see Fig. 1), where it drops to less than ∼3σ even for the brightest targets, respectively. The effect is more severe in the wavelength range λ > 7200 Å where many sky emission lines happen to be blended.

The procedure relies on the assumption that the morphological parameters do not change substantially as a function of the wavelength, something which is not completely true, since colour gradients are expected in all the galaxies. But, if they change, we expect this effect to have a minim impact in the photometry derived with GALFIT. Thus, if we use the morphological parameters derived by applying GALFIT to the F850LP band and we force the fitting procedure to use them for deriving the photometry at any other band, the recovered flux should be basically the same as when we let GALFIT fit these parameters freely. Although our previous experiments shown that this is the case (e.g. García-Lorenzo et al. 2005), we have also tested this hypothesis here, as described in Appendix B. In any case, the method is not strongly sensitive to this assumption, as described in Sánchez et al. (2006a). In principle, it is possible to perform the extraction procedure using the parameters derived from the morphological analysis as an initial guess, and letting GALFIT to derive the correct ones for each wavelength. In this case, the recovered spectra are noisier and in the residual data cube there is clear evidence of not correctly extracted structure.

3.5 Redshift determination

We determined the redshift of each detected galaxy in the field of view of our IFS data by comparing its spectrum with synthetic models for single stellar populations (SSP) obtained from Bruzual

& Charlot (2003). We will describe later in detail which models were used. We manually tuned the redshift of the model matching the different absorption features, including the Balmer lines (Hβ, Hγ, Hδ), the different Fe and Mg lines covered by our spectral range, as well as spectral features, like the 4000-Å break. Due to the spectral resolution of our IFS data, and the signal-to-noise ratio of our targets, we do not expect to have an accuracy better than 0.001 in the redshift determination. We derived realisable redshifts for 31 galaxies, 28 of them at the redshift of the cluster ($z = 0.17 \pm 0.2$), one is a foreground galaxy ($z = 0.104$), and other two are background galaxies (both at $z \sim 0.426$). Table 4 lists the derived redshifts together with the identifications shown in Fig. 5 (that we will use throughout this paper) and the SExtractor identification listed in Table 3 to allow for direct comparison.

11 of the 28 galaxies were studied before by Le Borgne et al. (1992). The redshifts derived from our data are coincident with the reported in this article within the expected errors ($\sigma_z \sim 0.001$). We derive new redshifts for 17 galaxies, all of them compatible with the redshift of the cluster. These new galaxies have been included in Table 3. In total, the final sample of cluster members (28) is comparable with that one of previous similar studies, but with the advantage that no sample has been selected: our sample is complete within the field of view of our IFS data down to our detection limit. Of these galaxies, only six have been previous studied with enough quality spectroscopy to derive the properties of their stellar populations (Ziegler et al. 2001). Therefore, our sample will increase significantly our knowledge of the core of the cluster.

3.6 The CM diagram

Fig. 6 shows the rest-frame $B - V$ versus M_V CM diagram for those cluster members listed in Table 2, derived from the *HST*/ACS based photometric data described above. The absolute magnitudes were corrected for cosmological effects and we applied a k-correction based on the same SSP synthetic model. For each synthetic SSP model (described below) we derived the expected $B - V$ colours at the average redshift of the cluster and in the rest frame, deriving at the same time the V-band k-correction. An average relation between the observed and rest-frame colours and the k-correction was derived, and applied to the data shown in Fig. 6. Red solid circles indicate galaxies with Sérsic index $n > 2.5$ (E-type), while green stars indicate those with $n < 1.75$ (L-type). Orange solid squares indicate galaxies with Sérsic indices in between those values, corresponding to intermediate galaxies. The cD galaxy is indicated with an orange open cross, being the brightest object in the field. We prefer to label it with a different symbol since it is well known that cD galaxies do not follow a Sérsic profile of any index, showing a flatter and more extended light profile in the outer regions (e.g. Oemler 1976). Open circles indicate the galaxies within the field of view of our IFS, with redshifts listed in Table 4. The big open square indicates the only galaxy with a high asymmetry index.

3.6.1 Morphological segregation

To our knowledge this is the first time that a morphologically segregated CM diagram is shown for confirmed cluster members. In previous works (e.g. Smail et al. 2001) only cluster galaxy candidates have been shown. The morphologies, based on the Sérsic indices listed in Table 3, break down as: 11 E-type, 19 intermediate and 29 L-type. If we consider as E-type galaxies to be all the objects

Table 4. Summary of the parameters derived from the spectra.

IFU ID	SEXTRACTOR ID	z	Hβ	Mgb	Age (Gyr)	Metallicity Z	Mass (10^{10} M$_\odot$)
1	1	0.174	*1.6 ± 0.1*	*3.0 ± 0.1*	9.8 ± 2.8	0.019 ± 0.011	102.1 ± 2.6
2	512	0.179	2.1 ± 0.1	3.4 ± 0.1	12.0 ± 3.4	0.025 ± 0.014	74.6 ± 2.8
3	501	0.163	1.1 ± 0.1	4.2 ± 0.2	12.9 ± 3.6	0.046 ± 0.026	39.5 ± 2.0
4	554	0.175	2.8 ± 0.1	3.6 ± 0.1	12.1 ± 3.4	0.025 ± 0.014	67.9 ± 3.3
5	555	0.181	1.4 ± 0.1	4.1 ± 0.2	11.6 ± 3.2	0.032 ± 0.018	36.2 ± 2.2
6	2	0.181	1.5 ± 0.6	6.1 ± 0.9	12.7 ± 3.6	0.045 ± 0.025	75.7 ± 4.6
7	509	0.184	*1.0 ± 0.1*	*3.0 ± 0.1*	9.9 ± 2.8	0.019 ± 0.011	17.2 ± 1.2
8	570	0.184	*1.5 ± 0.2*	*2.3 ± 0.7*	12.7 ± 3.6	0.045 ± 0.025	39.9 ± 2.7
9	599	0.163	1.5 ± 0.1	4.4 ± 0.2	9.6 ± 2.7	0.019 ± 0.011	10.5 ± 0.8
11	658	0.172	2.2 ± 0.1	3.9 ± 0.1	9.5 ± 2.7	0.018 ± 0.010	11.5 ± 0.8
12	596	0.174	1.4 ± 0.1	4.9 ± 0.1	12.4 ± 3.5	0.024 ± 0.013	13.6 ± 1.2
13	462	0.179	3.2 ± 0.1	2.7 ± 0.2	4.5 ± 1.3	0.018 ± 0.010	7.8 ± 0.6
14	449	0.178	2.7 ± 0.1	2.8 ± 0.2	5.2 ± 1.4	0.009 ± 0.005	4.5 ± 2.3
15	511	0.162?	*1.0 ± 0.2*	2.5 ± 0.2	9.5 ± 2.7	0.001 ± 0.001	2.2 ± 0.3
16	643	0.167	*1.2 ± 0.1*	0.7 ± 0.3	9.7 ± 2.7	0.019 ± 0.011	4.1 ± 0.5
17	632	0.179	2.8 ± 0.3	3.0 ± 0.2	3.5 ± 1.0	0.009 ± 0.005	2.1 ± 0.3
18	549	0.172	–	*3.5 ± 0.3*	5.2 ± 1.4	0.009 ± 0.005	2.8 ± 0.4
20	560	0.180	*2.2 ± 0.2*	0.7 ± 0.4	9.7 ± 2.7	0.019 ± 0.011	1.8 ± 0.3
21	533	0.171	*1.2 ± 0.3*	*1.8 ± 0.3*	11.5 ± 3.2	0.031 ± 0.018	4.5 ± 0.7
22	603	0.171	–	2.7 ± 0.3	5.8 ± 1.6	0.003 ± 0.002	1.0 ± 0.2
24	619	0.159	3.1 ± 0.2	2.8 ± 0.5	11.4 ± 3.2	0.006 ± 0.003	1.5 ± 0.2
25	484	0.174	*1.2 ± 0.5*	0.9 ± 0.3	4.2 ± 1.7	0.007 ± 0.004	1.0 ± 0.2
26	513	0.180	3.8 ± 0.4	–	7.1 ± 2.0	0.019 ± 0.011	2.1 ± 0.5
27	659	0.168	–	–	12.8 ± 3.6	0.045 ± 0.025	1.8 ± 0.6
28	575	0.168	–	–	12.7 ± 3.6	0.044 ± 0.025	3.6 ± 0.9
29	574	0.168	2.3 ± 0.7	–	9.7 ± 2.7	0.008 ± 0.004	0.6 ± 0.2
38	431	0.170	–	*1.2 ± 0.4*	0.3 ± 0.1	0.007 ± 0.004	0.1 ± 0.1
41	507	0.168	–	–	5.8 ± 1.6	0.007 ± 0.004	0.6 ± 0.1

Uncertain values are written in italic.
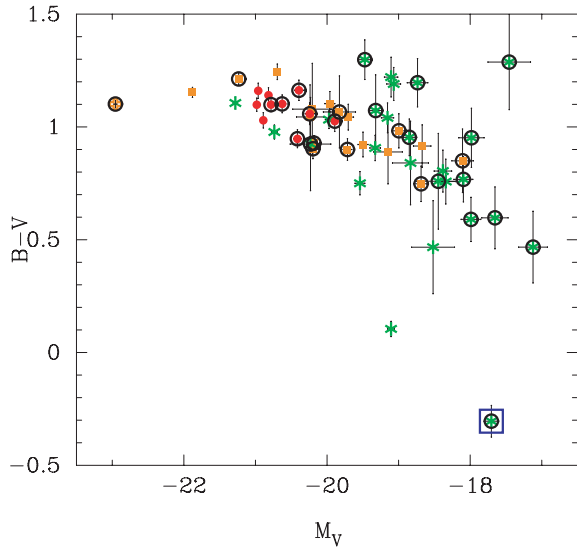
Figure 6. Rest-frame $B - V$ colour distribution as a function of absolute magnitude M_V for those cluster members listed in Table 2. Red solid circles indicate galaxies with Sérsic index $n > 2.5$ (E-type), while green stars correspond to objects with $n < 1.75$ (L-type). Orange solid squares indicate lenticular galaxies, with Sérsic indices in between both values. The cD galaxy is indicated with an orange open cross, being the brightest object in the field. Open circles indicate the 28 galaxies within the field of view of our IFS. The big open square indicates the only galaxy with a high asymmetry index.

with $n > 1.75$, they represent only a ~50 per cent of the total. For the complete subsample of galaxies covered within the IFU field of view, the morphologies break down as: 7 E-type, 8 intermediate and 13 L-type. Contrary to previous results (e.g. Smail et al. 2001; Ziegler et al. 2001) this indicates that the cluster population is not dominated by early-type galaxies, and there is an almost parity between early- and late-type galaxies.

Our approach to derive the morphologies is substantially different to in previous attempts, based on visual classifications. There is a considerable debate over the reliability of visual classifications of early-type galaxies (e.g. Dressler et al. 1997; Andreon 1998; Fabricant, Franx & van Dokkum 2000), and the ability to compare them with classifications based on profile analysis, like concentration and/or Sérsic indices. However, since there are no previous similar studies, we must compare with the existing ones. Ziegler et al. (2001) show visual morphological classifications of 19 of their 48 cluster members, based on WFPC/*HST* imaging. Their classification was performed by W. Couch, who classified them as 8E, 1 E/S0, 5 S0, 3 SB/0, 1 Sa and 1 Sab. Taking together all the E-type galaxies (E, E/S0 and S0), they account for a ~73 per cent of the total sample. Smail et al. (2001) presented morphological classification for 81 cluster candidates (33 with confirmed redshifts), based on the same analysis as Ziegler et al. (2001). Their morphologies break down as: 31 E, 3 E/S0, 28 S0, 5 Sa and 14 late-type spirals. Taking together all the E-type galaxies, they account for a ~76 per cent of the total sample. Even taking into account the different methods used to derive the morphologies, and the difficulties to compare them, it is clear that both Ziegler et al. (2001) and Smail et al. (2001) found fewer L-type galaxies than what we are finding.

Ziegler et al. (2001) selected galaxies using the previously existing redshift catalogue from Le Borgne et al. (1992) and defining a region in the *UBVI* colour space which was occupied by cluster members. Finally, only galaxies brighter than $I < 18.8$ mag were targeted by their spectroscopic survey. Although it was claimed that this selection places negligible restrictions on the stellar populations of the selected galaxies, and was made with the aim of rejecting the majority of background galaxies, it may have had an effect on the morphological segregation. The brightness cut in the *I* band implies that all the observed galaxies are brighter than $M_V < \sim -19.5$ mag, assuming an average $V - I$ colour of ~ 1.5 mag (Fukugita et al. 1995). If we apply such a cut in our sample (see Fig. 6), the morphologies break down as: 9 (7) E-type, 14 (5) S0's and 11 (2) L-type for the full (IFU) sample. This means a fraction of ~ 68 per cent (86 per cent) of E-type galaxies, in agreement with the results from Ziegler et al. (2001). Therefore, although visual classifications are not fully reproducible and may produce discrepancies in the morphological classification of individual objects, they agree with those ones based on Sérsic indices on a statistical base.

Smail et al. (2001) selected 81 cluster candidates based on a deep K_s-band survey ($K_s < 19$ mag), discarding those objects with clear stellar morphology, in too crowded areas and/or showing lensed morphologies. Assuming a $z - K_s$ colour of ~ 3 mag for the reddest objects, based on their own results for $I - K_s$ and an average $z - I$ colour of ~ 0.5 mag (Fukugita et al. 1995), they selected galaxies brighter than $z < \sim 22$ mag, a limiting magnitude similar to that of our IFU data. Therefore, a difference in the depth of both surveys is not the reason for the differences in the morphological segregation. We matched their cluster candidate sample with our full sample (listed in Table 3), finding 39 coincidences. For this subsample of confirmed cluster members the morphological segregation based on their analysis remains similar, with a ~ 82 per cent of E-type galaxies. Therefore, possible contaminations from non-cluster members are not the cause of the discrepancy. We examined the Sérsic indices of those 32 E-type galaxies. Of them, 10 have Sérsic indices lower than $n < 1.75$, being L-type galaxies following our scheme, and only seven have $n > 2.5$. Thus, the discrepancy is most probably due to the different criteria adopted for classifying the objects, illustrating the risks of direct comparisons between both methods. Statistically speaking visual classification gives the same distribution of galaxy types as profile fitting: on average, their E-type galaxies have larger Sérsic indices ($n \sim 2.6$) than their L-type ones ($n \sim 1.7$). However, it is well known that one-to-one cross-checking both methods give different results (e.g. Wolf et al. 2005), and profile analysis produces a more realisable and objective scheme for classifying objects.

3.6.2 Analysis of the CM diagram

The CM diagram contains extremely useful information to understand the nature of the cluster population. The $B - V$ colour is related to both age (strongly) and metallicity (weakly) of the dominant stellar population of the galaxy. On the other hand, the *V*-band absolute magnitude can be related to the stellar mass. Fig. 6 shows a bimodal distribution of early- and late-type galaxies in the CM diagram. E-type galaxies are (mostly) located in the brighter end of the distribution (no one is fainter than $M_V < \sim -20.5$ mag), covering a narrow range of colours ($1.9 < B - V < 2.2$). This is a well-known feature of early-type galaxies in clusters and it has been used for decades to select cluster candidates (e.g. Ziegler et al. 2001; Sánchez & González-Serrano 2002), and to trace the evolution of

the older population of cluster galaxies (e.g. Aragon-Salamanca, Ellis & Couch 1993).

On the other hand, L-type galaxies are distributed across a wide range of magnitudes with the brightest ones almost as red as the early-type galaxies, and the faintest ones bluer and covering a wider range of colours. For galaxies brighter than $M_V < -19.7$ mag there are no significant differences between the core members (galaxies in the IFU field of view), and the rest of the galaxies of the sample. For galaxies fainter than $M_V > -19.7$, it is found that the cluster core galaxies cover a wider range of colours, with more red galaxies. However, this difference may be due to a selection effect of the galaxy samples obtained from the literature. As indicated in Section 4.3 two of the 29 galaxies classified as L-type could be spheroidals on the basis of a visual inspection of the *HST*/ACS images. Both of them have red colours, $B - V \sim 0.9$ mag. However, they are not the redder L-type galaxies in their magnitude range. It is interesting to note here the location of the galaxy number 38 (IFU $_{ID}$), the only one showing a high asymmetry, being the bluest galaxy of our sample. This galaxy, at the east in Figs 2 and 3, is clearly identified as a merger in its latest stages, showing a clear tail to the south-west. Its spectrum, Fig. A1, shows strong Hβ, [O III]4959, 5007 and Hα emission lines and weaker [N II]6548, 6584, indicating a large amount of star formation. Its blue colours and spectrum also indicate the presence of an extremely young stellar population, far away from the global trend of the rest of the cluster members, as we will discuss below. Contrary to what is expected this galaxy is just at the nominal redshift of the cluster ($z = 0.17$, based on the emission lines), and considering its projected distance to the cluster centre (assumed to be the cD), it is not likely to be a fly-by object. To our knowledge it has escaped the attempt of previous studies, most probably because its morphology and colour automatically exclude it as a cluster candidate. Our IFU data lack the required spatial and spectral resolution to perform a more detail study of its properties.

A brief comparison of the CM distribution of the different kind of galaxies in the cluster, segregated by their morphology, indicates that E-type galaxies are more massive and have older and more metal rich stellar populations. L-type galaxies cover a wider range of masses, ages and metallicities, with the more massive ones being similar to the E-type galaxies, and the less massive ones younger and metal poorer. This result indicates that a bulk star formation process at high redshift may not be the unique mechanism to explain the population of the galaxies in the cluster. We will investigate it further in the next sections.

3.7 Galaxies ages and metallicities

We obtained spectra of the individual galaxies in the cluster with the aim of comparing their global spectroscopic properties with their morphological ones in a relative way, that is, only within the cluster. It is well known that the spectral energy distribution (SED) of simple stellar populations (chemically homogeneous and coeval stellar systems) depends on a set of first principles (e.g. initial mass function, star formation rate, stellar isochrones, element abundance ratios), to make it possible to generate synthetic stellar populations from them. This technique, known as evolutionary synthesis modelling (e.g. Tinsley 1980), has been widely used to unveil the stellar population content of galaxies by reconciling the observed SEDs with those predicted by the theoretical framework. Unfortunately the variation of different physical quantities governing the evolution of stellar populations produce similar effects in the integrated light of those systems, leading to a situation in which the observational data are affected by undesirable degeneracies, like the widely
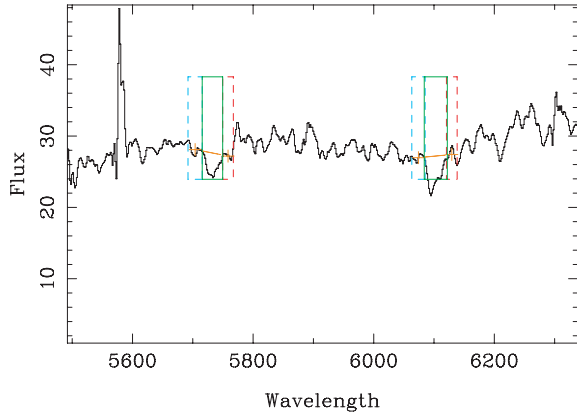
Figure 7. Example of the method used to derive the Hβ and Mgb line indices. The plot shows a detail of the spectrum of the galaxy number 2 (IFU$_{\mathrm{ID}}$), zoomed in on to the region of interest. For each absorption line the boxes indicate the regions where the adjacent continua are estimated (blue and red boxes) together with the region where the absorption is measured. The orange line indicates the adopted slope for the continuum. The strong feature at 5577 Å is the residual of the non-perfect subtraction of a night-sky emission line.

mentioned one between age and metallicity (e.g. O'Connell 1976; Aaronson et al. 1978; Worthey 1994a). The most widely used technique to compare galaxies with models is to measure certain line strength indices, on the Lick/IDS index system (Burstein et al. 1984; Faber et al. 1985; Burstein, Faber & González 1986; Gorgas et al. 1993; Worthey et al. 1994). People generally try to use a combination of indices that are most orthogonal in parameter space (e.g. age and metallicity; although see Cardiel et al. 2003 for a discussion of the impact of random errors in the selection of the best combination of indices). Following the Lick/IDS definitions, for our study we have chosen Hβ as a primary age indicator, and the Mgb index as a metallicity indicator. We use the Mgb index rather than the more conventional [MgFe] one, because both we and Ziegler et al. (2001) are unable to derive realisable Fe indices for most of the galaxies. This diagram has the drawback that the models based on solar abundance ratios do not match the Mg/Fe ratio observed in early-type galaxies (Thomas, Greggio & Bender 1999; Thomas, Maraston & Korn 2004). It is also well known that the ages derived from the grid are clearly uncertain in an absolute sense. However, we are primarily interested in a relative comparison of the ages and metallicities of the galaxies in the cluster, and in this sense the diagram is valid.

As we will discuss below, a proper estimate of those indices requires high signal-to-noise ratio spectra, and may be strongly affected by the instrumental and systemic velocity dispersions, the presence of weak emission lines that fill the absorptions (specially important in the case of Hβ), and the presence of high residuals corresponding to the removal of nearby sky emission lines.

3.7.1 Analysis of line-strength indices

We derive the Hβ and Mgb equivalent widths for our IFU sample using the bandpass definitions from the Lick index system revised by Trager et al. (1998), shifted to the redshift of each object. We used our own routines and checked the results with INDEXF.[2] Fig. 7 illustrates the procedure, showing a detail of the spectrum of galaxy

number 2 and the actual bandwidths used to derive each of the indices. The derived results are listed in Table 4, together with the error estimates (computed as explained below). We only list the positive values, since a negative equivalent width means emission, and not absorption. In most of the cases these negative values are found in faint targets, and are simply due to low signal-to-noise ratio of the spectra. However, in a few cases they indicate real emission lines, like the strong emission lines of galaxy number 38 (the merger) or fainter ones, like in galaxies numbers 18 and 22. In these three cases it is possible to derive realisable Mgb indices, but unreliable Hβ ones. On the other hand, there are a few objects (16, 20, 21 and 25), with too low Mgb equivalent widths for their Hβ ones. A visual inspection of their spectra, and a trace back to the raw data shows that they show cross-talk contamination from ThAr emission lines obtained in adjacent calibration fibres, which unfortunately lies in the regime of the Mgb absorption. For other four galaxies (numbers 1, 7, 8 and 15) both Hβ and Mgb seem to be too low. Galaxy number 1 is the cD, a kind of galaxy with well-known deviations of the metacillity sensitive indices (e.g. Cardiel et al. 1998). A visual inspection of its spectrum in the Hβ region indicates possible emission that fill the absorption. A similar inspection of the spectra of galaxy numbers 7 and 8 shows clear contaminations of sky emission-line residuals in the adjacent regions to the Hβ absorption band. Finally, galaxy number 15 has an uncertain redshift determination, which strongly affects the derived indices. All these objects have been excluded from further analysis based on line indices. Of the six galaxies in common with Ziegler et al. (2001), five have line-strength indices in common. In both cases, the strengths of Hβ and Mgb agree within ±0.6 Å, which is far beyond the estimated errors of both studies. However, such differences are expected on the basis of the different methods used to derive the strength of the line indices that may strongly affect the results.

We estimated the errors using Monte Carlo simulations of each spectrum, in the following way: first we derive for each spectrum the best matched single stellar population model, as we will describe in the next section. This model is included in Fig. A1. Then, we subtract the model from the spectrum, and derive the absolute value of the difference for each wavelength. Finally, we smooth this *residual* spectrum with a 10 pixels width median-box filtering. This smoothing was performed to reproduce as much as possible the noise cross-correlation pattern between adjacent pixels. The width was selected to match the spectral resolution, since we consider that this is the range of pixels where the cross-correlation of the noise is stronger. We consider that this rather complex method to estimate the errors is a better representation of the variance than the much simpler approach that would be to create a variance spectrum based on the estimated accuracy of our spectrophotometry (Section 2.1 and Appendix B). The reason for that is that using this latter approach we would not take local effects in the variance, like unperfections in the sky subtraction, cross-talk contaminations and inaccuracies on the reduction process. Using the adopted *variance* and our original spectrum we created 100 simulated spectra. The s.d. of the resulting equivalent widths are assumed to be the errors of our measurements. Line indices, for galaxies with velocity dispersions larger than 200 km s^{-1} (derived from the fitting to SSP models, as described below), are finally corrected as in Jablonka, Gorgas & Goudfrooij (2002) by using similar coefficients (Jablonka, private communication).

The final useful data set comprises line indices for 26 objects, 12 of them corresponding to our IFU sample. Fig. 8 shows the age–metallicity diagnostic diagram using Hβ as a primary age indicator and Mgb as a metallicity indicator. The symbols are similar to those

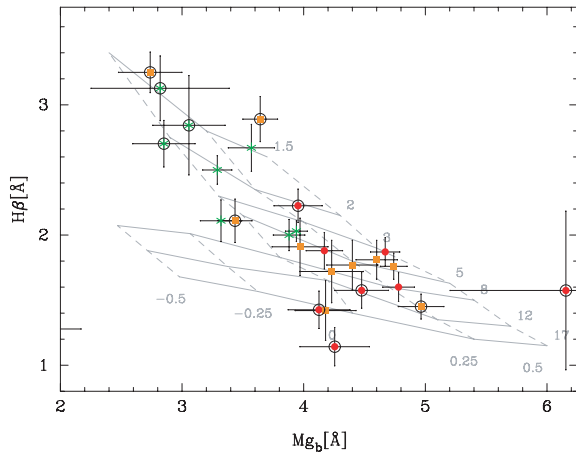[2] http://www.ucm.es/info/Astrof/software/indexf/

Figure 8. Age–metallicity diagnostic diagram using Hβ as a primary age indicator and Mg*b* as a metallicity indicator. The symbols are similar to those ones in Fig. 6. Overplotted is a grid of SSP models from Worthey (1994b). 'Horizontal' lines follow constant age (Gyr), 'vertical' lines constant metallicity ([M/H]). Each line is labelled with its corresponding age/metallicity.

in Fig. 6, including both our determined equivalent widths and those obtained by Ziegler et al. (2001). Overplotted is a grid of SSP models from Worthey (1994b). 'Horizontal' lines follow constant age, 'vertical' lines constant metallicity. Even though there are in the literature more recent evolutionary synthesis model predictions suitable for our purposes (e.g. Vazdekis et al. 2003; Bruzual & Charlot 2003; Thomas et al. 2004), here we are using the classical Worthey (1994b) models because we are just interested in a differential analysis of our data (i.e. the absolute derived ages and metallicities should not be taken literally) and we can perform a direct comparison with the results published by Ziegler et al. (2001). Ziegler et al. (2001) already noticed that E-type galaxies in this cluster cover a wide range of parameters as shown in Fig. 8, much wider than similar samples in the local universe (e.g. Kuntschner et al. 2001). We confirm this conclusion, since the new galaxies have increased the range of covered parameters. The bulk of the galaxies show lower metallicities and younger ages at a fixed metallicity compared to the ones in the local universe. They suggested that these differences may be due to variations in the average masses of the two galaxy samples, in the sense that more massive galaxies tend to be older.

The Ziegler et al. (2001) sample lacks enough L-type galaxies to draw a clear conclusion on the dependence of these parameters on the morphology. With the new sample it is possible to see that L-type galaxies are found towards younger ages, on average, than E-type galaxies at any fixed metallicity. On the other hand they seem to cover the same range of metallicities at any fixed age. These conclusions have to be taken with care, since most of our L-type galaxies are, at the same time, less luminous and therefore less massive than our E-type ones (Fig. 6). Therefore, if there is a correlation between the age and the mass, as suggested by Ziegler et al. (2001), this trend may affect both the E- and L-type galaxies, and explain our results. We will further investigate this possibility below.

3.7.2 Fitting to single stellar population models

Cardiel et al. (2003) already showed how sensitive the derivation of physical parameters from line indices is to the signal-to-noise ratio of the spectra. They concluded that using the full spectrum, when possible, one can derive better parameters, for a similar signal-to-

noise ratio. In the previous section we have seen that even for high signal-to-noise ratio spectra local contaminations from emission lines, both from the object and/or residuals from the sky or cross-talk from calibration fibres can strongly affect the derived indices.

To extract the maximum information for the maximum number of objects we fitted each spectrum from our IFU sample with synthetic SSP models. Models were created using the GISSEL code (Bruzual & Charlot 2003), assuming a Salpeter (1955) IMF (the use of a Chabrier (2003) will not modify the results), for different ages and metallicities. We create 72 models covering a discrete grid of 12 ages (5, 25, 100, 290, 640 Myr, 0.9, 1.4, 2.5, 5, 11, 13 and 17 Gyr), and six metallicities (Z = 0.0001, 0.0004, 0.004, 0.008, 0.02 and 0.05). Each spectrum was then fitted to each of the 72 models using FIT3D (Sánchez et al. 2006b). This code resamples the model to the resolution of the data, convolve it with a certain velocity dispersion, shift it to the redshift of the target and scale it to match the data set by a χ^2/ν minimization scheme. Therefore, for each SSP model, these are the three free parameters in the fitting process: velocity dispersion, redshift and a scaling factor related to the luminosity. The redshift of the object was fixed to reduce the degrees of freedom. Only the spectral region at wavelengths bluer than 7200 Å was used in this analysis. At redder wavelengths the strong night-sky emission lines and the telluric absorptions have not properly been corrected for in our reduction process, and strong residuals are seen in the spectra. Wavelength regions possibly affected by imperfect sky emission-line subtraction were also masked. We derived the velocity dispersions for each object spectrum in the fitting process, including both the intrinsic and instrumental ones. We cannot perform an accurate correction of the instrumental effects because we lack the proper comparison observations of velocity calibration stars during the night. This prevents us to use them as a mass indicator (e.g. Ziegler et al. 2001), using them only to correct the strength of the line indices, when required. The corrected velocity dispersions range between ∼100–400 km s^{-1}, and despite the lack of accuracy of our derived velocity dispersions they agree with the ones derived by Ziegler et al. (2001), for the six objects in common.

We obtain for each spectrum a grid of 72 χ^2/ν, each one corresponding to an age–metallicity pair model. Fig. 9 illustrates the result of the fitting technique. It shows a grey-scale of the χ^2/ν map derived after fitting the spectrum of galaxy number 2 to the grid of models, each one corresponding to an age–metallicity pair. Similar results are found for the rest of the objects. In the fitting procedure we assumed a simple rms of the flux as an estimation of the uncertainties in the spectra, to derive the χ^2/ν. Therefore these values
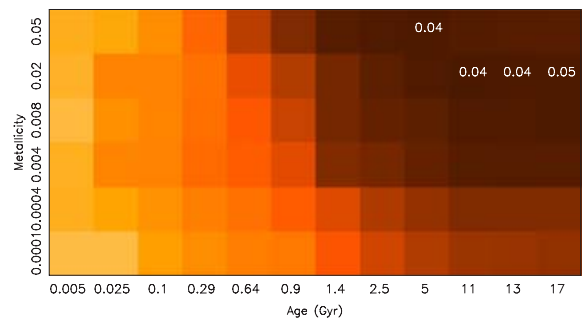

Figure 9. Grey-scale image of the 2D distribution of χ^2/ν derived from the fitting of a single galaxy spectrum to a grid of SSP models of different ages and metallicities. Dark colours indicate lower χ^2/ν (i.e. better fits), while light colours indicate higher vales (i.e. worse fits). The χ^2/ν of the four best fits are labelled. The plotted example corresponds to the second brightest galaxy in our field of view (ID = 2 in Table 4).

are not valid to compare the results of the fit for different objects, and just to perform internal comparisons between the results of the fit for the same object. The χ^2/ν of the four best fits are indicated in the figure. In general it is not possible to distinguish which is the best-fitting model among the best four. Therefore, we estimate the age and metallicity of each object by averaging the ages and metallicities of the four best models, weighted by the inverse of the corresponding χ^2/ν values. Errors for the estimated parameters are derived by Monte Carlo simulations: for each spectrum we estimate the *variance* spectrum as described above. Then we created 30 simulated spectra, using as input the original spectrum and adding noise following the estimated *variance*. For each of the 30 simulated spectra we run the fitting process over the 72 models (i.e. 2160 fits per input spectrum), and the age and metallicity are derived following the recipe described above. The s.d. of the recovered distribution of ages and metallicities for the simulated spectra is considered as a good estimate of the error of the measured parameters for the input spectrum. The final errors for the ages and metallicities are computed co-adding quadratically these estimated errors to the s.d. of the values for the four best models. The results from this procedure are listed in Table 4.

The method relies on certain assumptions: (i) we consider that the use of the full spectrum is a better method to recover the age and the metallicity of the main stellar population than just using the line indices and (ii) we consider that our spectrophotometric calibration is stable from blue to red, that is, that the shape of the spectra is well recovered. This is a sensitive assumption, since the whole method relies on it. To test its validity we compared our integrated spectra with the available broad-band photometry (Fig. A1). The photometric data set, derived from the *HST*/ACS data, covers the full optical wavelength range, from ~4700 to ~9000 Å, and in particular the wavelength range of our spectroscopic data. In most of the cases our spectroscopic data match pretty well with the broad-band photometric ones. Even more, the extrapolation of the data using the best-fitting SSP synthetic model reproduces also the expected photometry in wavelength ranges not covered by our spectroscopic data in most of the cases. Only galaxies number 9, 11, 16, 18, 22 and 24 show a slight missmatch (~2σ) between the extrapolated flux and the z_{850}-band photometry. If we take into account that the spectrophotometry seems to match for the rest of the bands and for the rest of the objects, we have strong arguments to consider that is also valid for these ones: we used an IFU, and therefore the flux calibration was performed only once for the full data set.

Finally, we assume that (iii) the adopted grid of models comprises a good representation of the expected stellar populations. We tried not to pre-judge the composition of the stellar population and cover the wider possible range of ages and metallicities. On the other hand, we must limit the number of input models for a reasonable performance of the fitting procedure. This imposes limitations on the sampling of the grid, and therefore, in the accuracy of the recovered age and metallicities. We must take that into account when drawing conclusions from our modelling.

3.7.3 The age–metallicity distribution

Fig. 10 shows the distribution of the metallicities as a function of age derived using the previously described fitting procedure for the galaxies in our IFU sample. The symbols are similar to the ones in Fig. 6. The size of the symbols indicates the mass (see below for a description of how it was estimated), with larger symbols for more massive objects. The merging galaxy (IFU$_{ID}$ = 38), is not visible in this plot, since the derived age for its stellar population, ~250 Myr, is far from the average of the rest of the sample. This result is expected
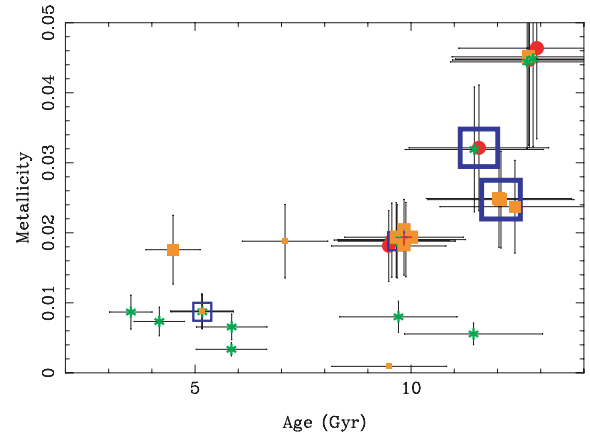

Figure 10. Distribution of the metallicities as a function of age derived by the fitting procedure for the 28 galaxies our IFS sample. The symbols are similar to those ones in Fig. 6. The size of the symbols indicates the mass, with larger symbols for more massive objects. All the E-type galaxies ($n > 2.5$), and most of the $n > 1.75$ ones have stellar populations older than ~9 Gyr and a wide range of metallicities, $0.02 < Z < 0.05$.

due its $B - V$ colour, and the strong star formation process that is derived from the strength of the emission lines on its spectrum. In this particular case a SSP model is not a good enough to describe the expected mix of populations resulting from a merging process, with at least an underlying stellar population, and a younger one resulting from the induced star formation process.

If we compare this figure with the Hβ–Mgb distribution shown in Fig. 8 evident differences can be seen. However, a direct comparison has to be done with care. First, the absolute ages and metallicities derived from both figures cannot be compared, since they come from completely different SSP models. We used the Worthey (1994b) models in the previous figure to be consistent with Ziegler et al. (2001), while the models used in the fitting procedure are derived from the GISSEL code (Bruzual & Charlot 2003). However, relative comparisons between the different galaxies are possible, in principle. One needs to take into account that in Fig. 8 we only represent 12 of the 27 objects shown in the current plot, that is, mostly the brightest ones. On the other hand, the objects from Ziegler et al. (2001) are not plotted in the current figure. However, the conclusions about the stellar populations of individual galaxies derived from both figures agree qualitatively: the galaxies with young and old stellar populations have young and old stellar populations in both figures, and the galaxies richer and poorer in metals are richer and poorer in both figures too.

We consider the current figure a more accurate representation of the real distribution of ages and metallicities of the galaxies in the cluster (or at least in the core). The plotted parameters were derived for the IFU sample, which is complete to our detection limit, without any pre-selection and any a posteriori exclusion. In general it is found that the galaxies with older stellar populations covers a wider range in metallicities, being more metal rich, on average, than the galaxies with younger stellar populations. This result does not agree with the trend between these two parameters found in field ellipticals, where galaxies with younger stellar populations are more metal rich (e.g. Trager et al. 2000). However, our sample comprises a large fraction of L-type galaxies. As in Fig. 6 we found a clear different behaviour for the E- and L-type galaxies. All the E-type galaxies with $n > 2.5$ (spheroidals), and most of the $n > 1.75$ ones (intermediate galaxies) have stellar populations older than ~9 Gyr, covering a wide range of metallicities, $0.02 < Z < 0.05$. On the

other hand, the L-type galaxies ($n < 1.75$), cover a much wider range of ages, from $\sim$3 Gyr to $\sim$13 Gyr (keeping in mind that the absolute ages have no meaning), and metallicities, $0.001 < Z < 0.05$. Interestingly, the L-type galaxies with the largest metallicities ($Z > 0.015$) seems to have similar ages as the E-type ones, and the L-type galaxies with smaller metallicities cover a wider range of ages. The most metal rich galaxies are the more massive ones (with larger symbols), and therefore, this result may indicate that more massive galaxies tend to be older whatever their morphologies. We will discuss that in detail below. This result is certainly not clear from Fig. 8.

3.8 Stellar populations and masses of the galaxies

In previous sections we have already seen that the masses of the galaxies are directly related to the nature of their stellar populations. The CM diagram, Fig. 6, shows that less luminous (and massive) galaxies show a wider range of colours than more luminous objects. The comparison of the Hβ-Mgb distribution of this cluster with that of the local universe, including more massive galaxies, makes Ziegler et al. (2001) think that there might be a trend of metallicities/ages with the mass of the objects. Fig. 10 shows that more massive galaxies are, on average, older and more metal rich. We investigate here the possible relations between the stellar populations and the morphology with the mass of the galaxies.

It is well known that the masses of spheroidal or early-type galaxies are directly related to their stellar velocity dispersions (σ), due to their nature. This parameter, directly accessible from the spectra, has indeed been used as a mass indicator for decades, leading to a set of well establish scaling relations when comparing it with different properties of the galaxies. Among these relations the most important ones are the luminosity–velocity dispersion relation or Faber–Jackson relation (Faber & Jackson 1976), the surface brightness, effective radius and velocity dispersion relation or Fundamental Plane (Djorgovski & Davis 1987; Dressler et al. 1987; Bender, Burstein & Faber 1992) and the Mg–velocity dispersion relation or Mgb-σ relation (Bender, Burstein & Faber 1993; Colless et al. 1999). These scaling relations have been used to compare between different populations of early-type galaxies at different redshifts (e.g. Ziegler et al. 2001), to trace the evolution of this kind of galaxies. For late-type galaxies similar relations are found when using the maximum rotating velocity, a parameter directly related with the mass of the rotating disc.

All these relations have a direct correspondence with relations between the mass and the different properties of the galaxies: The Faber–Jackson relation can be understood as a luminosity–mass relation, the Fundamental Plane as a mass-scale relation and the Mg-σ as a metallicity–mass relation. Our spectroscopic data lack the required resolution and signal-to-noise ratio for a proper determination of the velocity dispersion for most of the galaxies, therefore, we prefer to investigate these relations using the stellar masses of the galaxies. This approach has the advantage that we can explore at the same time all the galaxies of the sample independent of their morphology.

We estimate the stellar masses using the average relation found by Bell & de Jong (2001) between the mass-to-light ratio (M/L) for the B-band luminosity and the $B - V$ colour. For doing that we derive the rest-frame $B - V$ colours of our objects using the best-fitting SSP model described before, synthesizing the magnitudes by convolving the model with the filter responses, and obtaining the B-band absolute magnitude from our photometric data. It is important to note that the masses of Bell & de Jong (2001) are just relative values, calibrated under the assumption that spiral galaxies are in
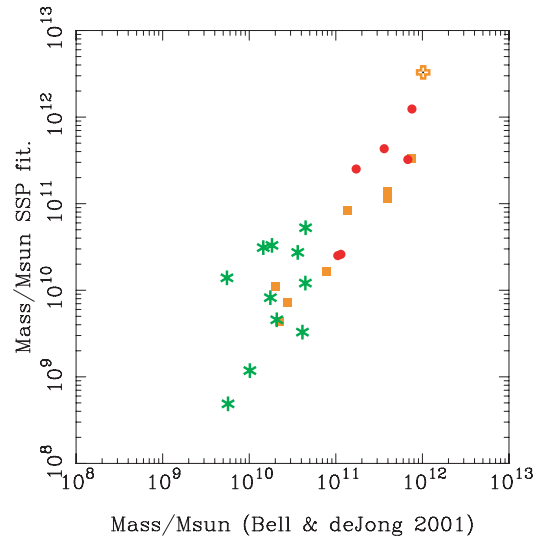

Figure 11. Distribution of the stellar masses for the galaxies of our sample derived from the results of the fitting procedure to SSP models along the stellar masses derived using the Bell & de Jong (2001) approximation.

a maximum-disc situation. However, this will not affect our results since we are interested in relative comparisons between different families of galaxies. This comparison is not affected by the use of a different method to estimate the masses, like the mass derived directly by the fitting procedure over an SSP (Fig. 11). The derived masses are listed in Table 4. The errors listed in the table were derived from the photometric errors in the B-band magnitudes listed in Table 2, and they do not include any other possible source of error (like the inaccuracy of the fitting process or the derived synthetic colours). However, we consider that this error dominates any other possible one. The masses of the objects range between $\sim 10^9$ and $\sim 10^{12}$ M$_{\odot}$, being the cD galaxy the most massive galaxy and the merging galaxy the least massive one.

3.8.1 The age–mass relation

Fig. 12 shows the age distribution as a function of stellar masses for the galaxies of our IFU sample. The symbols are similar to those in Fig. 6. The division of galaxies in terms of morphologies is remarkably similar to that of the CM relation (Fig. 6), although in the current plot the segregation between early- and late-type galaxies is much stronger. Most of the E-type galaxies ($n > 1.75$) and all the ones with $n > 2.5$ are more massive than $\sim 7 \times 10^{10}$ M$_{\odot}$ and have stellar populations older than $\sim$9 Gyr. On the other hand, all the L-type galaxies are less massive than this limit, and the ages of their stellar populations spread towards younger ages. There is no obvious trend of age with mass, but there is a lack of young stellar populations in massive galaxies. Since all of them are E-type ones, it is not possible to know if this deficit is due to the mass or the morphology of the galaxies. However, such a trend is expected, at least for field early-type galaxies. Recently Peletier et al. (in preparation) reported a trend between the age and the mass for field early-type galaxies based on data from the SAURON project (Bacon et al. 2001).

Fig. 13 illustrates this effect. It shows the distribution of Sérsic indices as a function of the stellar masses for the galaxies of our IFU sample. The symbols are similar to those in Fig. 6. There is a strong correlation between both parameters, in the sense that E-type galaxies are massive and L-type ones less massive. The relation is
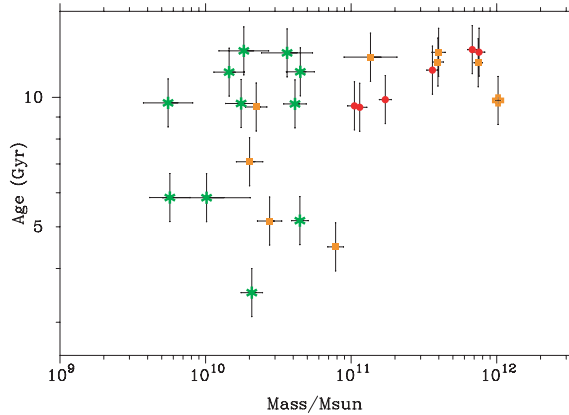
Figure 12. Distribution of ages along stellar masses for our galaxy sample. The symbols are similar to those ones in Fig. 6. There is a clear morphological segregation. L-type galaxies are less massive than $10^{11}\,M_\odot$, and have a wider range of ages than E-type galaxies.
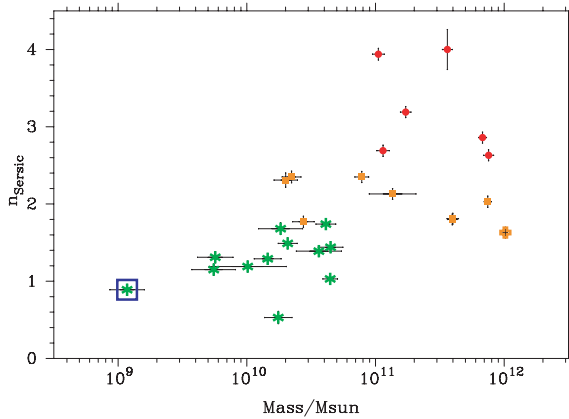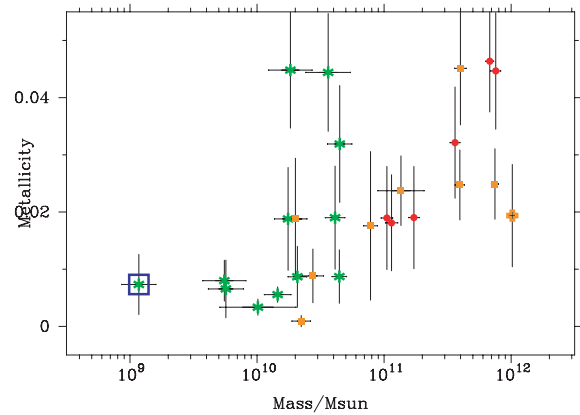

Figure 13. Distribution of Sérsic indices as a function of the stellar masses for the galaxies of our sample. The symbols are similar to those in Fig. 6. There is a clear trend in the sense that E-type galaxies are more massive than L-type ones.

clearer when masking the cD and the merger galaxies, for which the profiles are not well represented by the adopted model.

Similar results were already presented by Ziegler et al. (2001) for the early-type galaxies of A2218 in the outer regions. They compared the Hβ index with the stellar velocity dispersion finding that the fainter galaxies shows a larger scatter in their Hβ values, indicating a wide range of star formation histories. Our survey goes deeper, sampling galaxies much fainter (and less massive) that those ones studied by Ziegler et al. (2001), extending their conclusions to fainter regimes.

3.8.2 The metallicity–mass relation

As we pointed out above, the Mgb–σ relation can be understood as a metallicity–mass relation. Fig. 14 shows the distribution of the metallicities as a function of the stellar mass for the galaxies of our IFU sample. The symbols are similar to those ones in Fig. 6. As expected there is a clear correlation between both parameters ($r = 0.997$, $P > 99.99$ per cent), in the sense that massive galaxies of any kind are more metal rich than less massive ones. A similar result is found when using the mass derived by the fitting to SSP synthetic models, instead of the adopted one, based on the Bell &

Figure 14. Distribution of the metallicities as a function of stellar mass for the galaxies of our sample. The symbols are similar to those in Fig. 6. There is a clear correlation between both parameters, in the sense that more massive galaxies are more metal rich than less massive ones.

de Jong (2001) relation. Although the result is not surprising for the E-type galaxies, it is interesting that the L-type galaxies follow a similar relation, but with an offset. The trend between metallicity and mass seems to be universal for any kind of galaxy, despite of its morphology. However, for any fixed mass the L-type galaxies seem to be more metal rich than the E-type ones. This effect is not due to a difference in age of the stellar populations, since at equal age we observe a considerable range in metallicity. However, our sample is too reduced to draw firm conclusions.

4 DISCUSSION

The galaxy population of clusters in the local universe are dominated by early-type galaxies (E's and bulge-dominated spirals) Hubble & Humason (1931), Oemler (1974), with a reduced fraction of late-type galaxies (spirals, irregulars and mergers). There is a general agreement about the ages of the stellar populations in early-type cluster galaxies. It is well known that they show a strong CM relation at various redshifts consistent with passive evolution of stellar populations that formed at $z > 2$–3, with a slope due to the mass–metallicity relation (e.g. Stanford et al. 1997; Kodama et al. 1998; Stanford et al. 1998; Poggianti 2003). The spectroscopic features and the scaling relations, like the Fundamental Plane, the M/L, the Mgb–σ and the Faber–Jackson relations, explored at different redshift are also consistent with passive evolution of an old stellar population (e.g. Bender et al. 1996; van Dokkum & Franx 1996; van Dokkum et al. 2001; Kelson et al. 2001; Ziegler et al. 2001).

However, this apparently simple scenario for the evolution of early-type galaxies in clusters needs to be contrasted with another result. Fasano et al. (2000) show that there is a substantial morphological evolution in clusters: as the redshift decreases the S0 population tends to grow at the expense of spiral population, whereas the frequency of spheroidals remains almost constant. Therefore the population of early-type galaxies observed in distant clusters does not necessarily comprise all the early-type galaxies existing at $z = 0$ (Poggianti 2003). On the other hand, the blue galaxies observed in distant clusters, responsible of the Butcher–Oemler effect, must largely become red and fainter. There is strong evidence for a quenching of star formation in galaxies as a consequence of the infall in the cluster dense regions (Poggianti et al. 2001, 2004), although a previous starburst may be also present (Poggianti et al. 2004). For galaxies with a star formation history

typical of L-type, once truncated, it is expected that they become redder and fade by 0.5–1.5 mag in ~2–5 Gyr (Poggianti et al. 2004). Finally, although the spectrophotometric and the morphological evolution seems to be largely decoupled, it is expected that after longer time-scales there will a morphological transformation from pure L-type to bulge-dominated spirals (Fasano et al. 2000). All these results suggest that the early-type galaxies in clusters are composed of a mix of different stellar populations, with very different origins, contrary to the simple scenario drawn above.

How do our results compare with previous knowledge of the evolution of galaxies in clusters? The morphological distribution of the cluster members derived from our analysis is: 11 (7) E-type, 19 (8) lenticulars, and 29 (13) L-type, for our complete sample (our IFU sample). In percentages it is: 19 per cent (25 per cent) E-type, 32 per cent (29 per cent) lenticulars and 49 per cent (46 per cent) L-type. These fractions differ strongly with the estimated ones for clusters at similar redshifts: 30 per cent E-type, 50 per cent lenticulars and 20 per cent L-type (Fasano et al. 2000), showing a much larger fraction of late-type galaxies. Fasano et al. (2000) estimated these numbers based on images with limiting magnitudes of the order of $r \sim 20.2$–20.5 mag, that is, ~1.5–2 mag less deep than our current survey (taking into account the range of possible $r - z$ colours for any kind of galaxy at this redshift, from ~0 mag to ~0.6 mag, Fukugita et al. 1995). If we consider only the objects brighter than $z < 20$ mag, the new morphological segregation is: 9 (7) E-type, 16 (7) lenticulars and 16 (4) L-type. These percentages are within the values reported by (Fasano et al. 2000): 22 per cent (39 per cent) E-type, 39 per cent (39 per cent) lenticulars and 39 per cent (22 per cent) L-type. Therefore, there is an increase of the fraction of late-type galaxies at fainter magnitude regimes.

Looking at Figs 6 and 12 it is possible to identify two kinds of L-type galaxies in the faint magnitude regime: (i) a group of blue and faint galaxies, with young stellar populations (<8 Gyr), and (ii) another group of red and faint galaxies, with older stellar populations (>8 Gyr). The first ones are the kind of galaxies responsible for the Butcher–Oemler effect. Galaxies recently captured by the cluster, with relatively young stellar populations and traces of recent star formation processes. Due to their colours these galaxies would be detected in surveys in the optical/blue bands. The second group are the kind of galaxies predicted in the two-step evolution hypothesis for galaxies captured by clusters, where the star formation was quenched first, and then there was a slower morphological transformation (Poggianti et al. 2001; Poggianti 2003). As a first step the late-type galaxies fall into the cluster, and due to gas stripping the star formation process is abruptly interrupted (maybe after a short starburst process). Then, these galaxies become fainter and redder, while still showing a spiral shape.

Clusters with the highest fraction of blue galaxies shows signs of recent mergers, and there are larger fractions of star-forming galaxies in substructured than in relaxed clusters (e.g. Smail et al. 1998; Metevier, Romer & Ulmer 2000; Pimbblet et al. 2002). Theoretical simulations predict that the cluster mergers induces a starburst processes, due to the strong tidal forces involved (e.g. Moss & Whittle 2000), a similar effect of galaxy–galaxy interactions (e.g. Mihos & Hernquist 1996). Abell 2218 shows two clear peaks in the X-ray and galaxies distribution (McHardy et al. 1990), indicating that it most probably has suffered a recent (or ongoing) merging. This may account for the moderate Butcher–Oemler fraction of blue galaxies quoted in classical studies (~10 per cent Butcher & Oemler 1984).

Galaxies captured by the cluster may suffer similar tidal forces, which may induce an enhancement of the star formation process, previous to the quenching due to gas stripping (Poggianti 2003). The

location of the k + a (post-starburst) galaxies, and the strength of their Balmer absorption features strongly supports this hypothesis (Poggianti et al. 2004). To our knowledge, Abell 2218 is the only cluster at cosmological distances where HI is observed in emission (Zwaan, van Dokkum & Verheijen 2001), at the location of a spiral galaxy in the outer regions of the cluster. This galaxy is most probably an infalling spiral, consuming its gas reservoir with ongoing star formation (estimated SFR of <1.4 $M_\odot$ yr^{-1}). More spectacular is galaxy number 38 from our IFU sample, a blue disrupted galaxy at the nominal redshift of the cluster with a very little projected distance from the centre of the cluster. It is possible that this galaxy has been recently captured by the cluster, and that it is moving in an orbit perpendicular to the line of sight. If not, there should be a conspiracy between its cosmological redshift and line-of-sight velocity to compensate each other so that it appears to be at the nominal redshift of the cluster, which is an unlikely explanation. Its emission lines indicate a moderate amount of ongoing star formation, with a SFR ~ 6 $M_\odot$ yr^{-1}, derived from the Hα emission (Kennicutt 1983; Kennicutt, Tamblyn & Congdon 1994). No dust is derived from the Hα/Hβ ratio, ~2.9, nearly the nominal value for case B recombination. Its dominant stellar population has an age of ~250 Myr, which could be a feasible time-scale for the infalling process. Its morphology is similar to that one of a merger in its last stage, however, the strong tidal forces that may suffer during the infalling process may have produced the same effect. If the proposed scenario for the evolution of galaxies in cluster is true, this galaxy would be a good candidate for a progenitor of the observed 'k + a' galaxies at low redshift (Poggianti et al. 2004). In a recent study of Abell 2125, a dense cluster at $z \sim 0.247$, Owen et al. (2006) found a galaxy with strong emission lines (maybe even with an active galactic nucleus), blue colours, and a disturbed morphology. Although that galaxy is brighter than galaxy number 38, both systems seem to experience the same physical process.

Our results indicate that there is a correlation between the morphology and the mass, in the sense that less-massive galaxies are mostly L-type and more massive ones are mostly E-type (Fig. 13). This result is natural in the proposed scenario, where the morphological transformation between L-type to bulge-dominated spirals, and later to E-type galaxies is a consequence of consecutive merging processes. We have also found a clear correlation between the mass and the metallicity, in the sense that more massive galaxies are more metal rich (Fig. 14). This correlation is an extension of the well-known Mgb–σ relation for spheroidal galaxies, which seems to be independent of the galaxy morphology. Although we have a very reduced sample, it seems that L-type galaxies are more metal-rich than E-type ones at any fixed mass. Fig. 14 also indicates that the more metal rich L-type galaxies are never more metal than the E-type ones, being only less massive. To our knowledge this effect has not been previously reported in the literature, and it may well be an effect of the very reduce sample. If not, it may imply that the galaxies reach their maximum metallicity when they are still spirals, maybe due to the enhancement of the star formation rate when falling into the cluster, and that they later evolve to more massive bulge-dominated spirals and E-type galaxies keeping this metallicity.

5 CONCLUSIONS

We obtained deep IFS data ($I_{lim} \sim 21.4$ mag) covering a field of view of $\sim 74 \times 64$ arcsec^2 centred on the core of the galaxy cluster Abell 2218, sampling the wavelength range 4650–8000 Å with a resolution of ~10 Å (FWHM). Combining these data with a deep *HST*/ACS F850LP-band image ($z_{lim} \sim 28$ mag), and ground-based

and *HST*/WFPC photometric data, we have obtained the following results.

(i) Morphological parameters of all the galaxies in the field of view of the *HST*/ACS image down to $z < 22.5$ mag were obtained, based on an automatic procedure using GALFIT.

(ii) The integrated spectrum of each of the 43 objects detected in the IFU data cube was obtained, using a modelling technique for IFS (GALFIT3D), which ensures a proper deblending of multiple components in crowded fields.

(iii) Of the detected objects, 28 were classified as cluster members based on their redshifts. They comprise the first volume and flux-limited sample of confirmed cluster members obtained for the core of this cluster. We need to remark that the sample was obtained without any pre-selection based on morphology, colours or magnitudes.

(iv) By combining the different previous redshift and photometric surveys with our new morphological information an extended sample of 59 cluster members was created, 31 of them sampling the outer regions of the cluster (out of the core).

(v) The CM diagram of the full sample of confirmed cluster members, as a function of the morphology, was analysed. We have found that the fraction of early-type galaxies is lower than previously reported, most of them being red and luminous galaxies. On the other hand, the L-type galaxies spread over a wider range of colours and luminosities with respect to the E-type ones and previously published catalogs.

(vi) There is no significant difference between the CM distributions of the galaxies in the core of the cluster and in the outer regions if one distinguishes between different morphologies. If any, we found a few more L-type faint and red galaxies in the core. However, this may be due to the biases of the pre-selection of candidates in the samples obtained from the literature (in the outer regions).

(vii) A strongly distorted blue galaxy is found in projection at the core of the galaxy cluster. Its redshift corresponds to the nominal redshift of the cluster, and therefore, it is more likely that it is physically located in the core. A visual inspection of the object indicates that it looks like a merger in an advance stage of evolution, dominated by a young stellar population. However, if we are observing it in the moment of being captured by the cluster, the strong tidal forces that it is suffering may produce the observed disruption on its morphology.

(viii) The analysis of the age and metallicity of a reduced subsample of galaxies (24 galaxies, 12 core members) based on line indices indicates that L-type galaxies on average spread towards younger ages than E-type ones. On the other hand, they seem to cover the same range of metallicities at any fixed age.

(ix) The age and metallicity of each galaxies in the core of the cluster were derived by a fitting procedure of its integrated spectrum to single stellar population models. The age–metallicity diagram of these galaxies indicates too that L-type galaxies cover a clearly wider range of ages, and a slightly wider range of metallicities. The more massive L-type galaxies seem to have similar ages and metallicities than the E-type ones, while the less massive ones tend to be younger and less metal rich.

(x) The distribution of ages and Sérsic indices as a function of the stellar masses of the core members shows that L-type galaxies are less massive on average. They spread over a wider range of ages, but it is not possible to determine if this is due to their morphologies or masses. On the other hand, more massive galaxies tend to have older stellar populations and they are all early-type galaxies.

(xi) There is a clear trend between the metallicity and the mass, in the sense that more massive galaxies are more metal rich. This trend is just a change of coordinates of the well-known Mgb–σ relation for the early-type galaxies. However, we found that this trend is also present for the L-type galaxies, but with an offset: they are more metal rich than E-type galaxies at any fixed mass.

Our results agree with the proposed two-step scenario for the evolution of galaxies in clusters (e.g. Poggianti 2003), in which we have (i) a primordial population of early-type galaxies formed at early epochs with stellar populations that are mostly old, and (ii) a new population of L-type galaxies that are captured by the cluster, infalling, suffering a short enhancement of the star formation that is later quenched by the interaction with the environment. The galaxies then evolve passively, becoming redder and fainter, while keeping the spiral morphology. The discs dim due to the lack of newly formed stars, and the galaxies become bulge-dominated spirals, after longer time-scales. Later galaxy–galaxy interactions and dry merging processes build up new massive spheroidal galaxies.

REFERENCES

Aaronson M., Cohen J. G., Mould J. R., Malkan M., 1978, ApJ, 223, 824
Abell G. O., Corwin H. G., Olowin R. P., 1989, ApJS, 70, 1
Andredakis Y. C., Peletier R. F., Balcells M., 1995, MNRAS, 275, 874
Andreon S., 1998, ApJ, 501, 533
Aragón-Salamanca A., Ellis R. S., Couch W. J., Carter D., 1993, MNRAS, 262, 764
Bacon R. et al., 2001, MNRAS, 326, 23
Balogh M. L., Morris S. L., Yee H. K. C., Carlberg R. G., Ellingson E., 1999, ApJ, 527, 54
Barazza F. D., Binggeli B., Jerjen H., 2003, A&A, 407, 121
Barazza F. D. et al., 2006, ApJ, 643, 162
Bell E. F., de Jong R. S., 2001, ApJ, 550, 212
Bell E. F. et al., 2004, ApJ, 600, L11
Bell E. F. et al., 2006, ApJ, 640, 241
Bender R., Burstein D., Faber S. M., 1992, ApJ, 399, 462
Bender R., Burstein D., Faber S. M., 1993, ApJ, 411, 153
Bender R., Kormendy J., Dehnen W., 1996, ApJ, 463, L51
Bertin E., Arnouts S., 1996, A&AS, 117, 393
Bruzual G., Charlot S., 2003, MNRAS, 344, 1000
Burstein D., Faber S. M., Gaskell C. M., Krumm N., 1984, ApJ, 287, 586
Burstein D., Faber S. M., González J. J., 1986, AJ, 91, 1130
Butcher H., Oemler A., 1978a, ApJ, 219, 18
Butcher H., Oemler A., 1978b, ApJ, 226, 559
Butcher H., Oemler A., 1984, ApJ, 285, 426
Butcher H., Wells D. C., Oemler A., 1983, ApJS, 52, 183

Cairós L. M., Vílchez J. M., González Pérez J. N., Iglesias-Páramo J., Caon N., 2001, ApJS, 133, 321

Cardiel N., Gorgas J., Aragón-Salamanca A., 1998, MNRAS, 298, 977

Cardiel N., Gorgas J., Sánchez-Blázquez P., Cenarro A. J., Pedraz S., Bruzual G., Klement J., 2003, A&A, 409, 511

Chabrier G., 2003, PASP, 115, 763

Coe D., Benítez N., Sánchez S. F., Jee M., Bouwens R., Ford H., 2006, AJ, 132, 926

Colless M., Burstein D., Davies R. L., McMahan R. K., Saglia R. P., Wegner G., 1999, MNRAS, 303, 813

Conselice C. J., Bershady M. A., Dickinson M., Papovich C., 2003, AJ, 126, 1183

Couch W. J., Sharples R. M., 1987, MNRAS, 229, 423

Couch W. J., Ellis R. S., Sharples R. M., Smail I., 1994, ApJ, 430, 121

Covone G., Kneib J.-P., Soucail G., Richard J., Jullo E., Ebeling H., 2006, A&A, 456, 409

de Vaucouleurs G., de Vaucouleurs A., Corwin J. R., 1976, Second Reference Catalogue of Bright Galaxies. University of Texas Press, Austin

Djorgovski S., Davis M., 1987, ApJ, 313, 59

Dressler A., Gunn J. E., 1983, ApJ, 270, 7

Dressler A., Lynden-Bell D., Burstein D., Davies R. L., Faber S. M., Terlevich R., Wegner G., 1987, ApJ, 313, 42

Dressler A., Oemler A. J., Butcher H. R., Gunn J. E., 1994, ApJ, 430, 107

Dressler A. et al., 1997, ApJ, 490, 577

Dressler A., Smail I., Poggianti B. M., Butcher H., Couch W. J., Ellis R. S., Oemler A., Jr, 1999, ApJS, 122, 51

Faber S. M., Jackson R. E., 1976, ApJ, 204, 668

Faber S. M., Friel E. D., Burstein D., Gaskell C. M., 1985, ApJS, 57, 711

Fabricant D., Franx M., van Dokkum P., 2000, ApJ, 539, 577

Fasano G., Poggianti B. M., Couch W. J., Bettoni D., Kjærgaard P., Moles M., 2000, ApJ, 542, 673

Fritz A., Ziegler B. L., Bower R. G., Smail I., Davies R. L., 2005, MNRAS, 358, 233

Fukugita M., Shimasaku K., Ichikawa T., 1995, PASP, 107, 945

García-Lorenzo B., Sánchez S. F., Mediavilla E., González-Serrano J. I., Christensen L., 2005, ApJ, 621, 146

Gorgas J., Faber S. M., Burstein D., González J. J., Courteau S., Prosser C., 1993, ApJS, 86, 153

Hubble E. P., 1926, ApJ, 64, 321

Hubble E., Humason M. L., 1931, ApJ, 74, 43

Jablonka P., Gorgas J., Goudfrooij P., 2002, Ap&SS, 281, 367

Johnson H. L., Morgan W. W., 1953, ApJ, 117, 313

Kelson D. D., Illingworth G. D., van Dokkum P. G., Franx M., 2000, ApJ, 531, 137

Kelson D. D., Illingworth G. D., Franx M., van Dokkum P. G., 2001, ApJ, 552, L17

Kelz A., Verheijen M. A. W., Roth M. M. et al., 2006, PASP, 118, 129

Kennicutt R. C., 1983, ApJ, 272, 54

Kennicutt R. C., Tamblyn P., Congdon C. E., 1994, ApJ, 435, 22

Kodama T., Arimoto N., Barger A. J., Aragón-Salamanca A., 1998, A&A, 334, 99

Kristian J., Sandage A., Westphal J. A., 1978, ApJ, 221, 383

Kuntschner H., Lucey J. R., Smith R. J., Hudson M. J., Davies R. L., 2001, MNRAS, 323, 615

Le Borgne J. F., Pelló R., Sanahuja B., 1992, A&AS, 85, 87

McHardy I. M., Stewart G. C., Edge A. C., Cooke B., Yamashita K., Hatsukade I., 1990, MNRAS, 242, 215

Metevier A. J., Romer A. K., Ulmer M. P., 2000, AJ, 119, 1090

Mihos J. C., Hernquist L., 1996, ApJ, 464, 641

Moore B., Katz N., Lake G., Dressler A., Oemler A. Jr, 1996, Nat, 379, 613

Moss C., Whittle M., 2000, MNRAS, 317, 667

O'Connell R. W., 1976, ApJ, 206, 370

Oemler A. J., 1974, ApJ, 194, 1

Oemler A. Jr, 1976, ApJ, 209, 693

Owen F. N., Keel W. C., Wang Q. D., Ledlow M. J., Morrison G. E., 2006, AJ, 131, 1974

Peng C. Y., Ho L. C., Impey C. D., Rix H., 2002, AJ, 124, 266

Pimbblet K. A., Smail I., Kodama T., Couch W. J., Edge A. C., Zabludoff A. I., O'Hely E., 2002, MNRAS, 331, 333

Poggianti B. M., 2003, Ap&SS, 285, 121

Poggianti B. M., Smail I., Dressler A., Couch W. J., Barger A. J., Butcher H., Ellis R. S., Oemler A. J., 1999, ApJ, 518, 576

Poggianti B. M. et al., 2001, ApJ, 563, 118

Poggianti B. M., Bridges T. J., Komiyama Y., Yagi M., Carter D., Mobasher B., Okamura S., Kashikawa N., 2004, ApJ, 601, 197

Rakos K., Dominis D., Steindling S., 2001, A&A, 369

Roth M. M., Kelz A., Fechner T. et al., 2005, PASP, 117, 620

Salpeter E. E., 1955, ApJ, 121, 161

Sánchez S. F., 2004, Astron. Nachr., 325, 167

Sánchez S. F., 2006, Astron. Nachr., 327, 850

Sánchez S. F., Cardiel N., 2005, Calar Alto Newslett., 10 (online only publication)

Sánchez S. F., González-Serrano J. I., 2002, A&A, 396, 773

Sánchez S. F. et al., 2004a, ApJ, 614, 586

Sánchez S. F., García-Lorenzo B., Mediavilla E., González-Serrano J. I., Christensen L., 2004b, ApJ, 615, 156

Sánchez S. F., García-Lorenzo B., Jahnke K., Mediavilla E., González-Serrano J. I., Christensen L., Wisotzki L., 2006a, New Astron. Rev., 49, 501

Sánchez S. F., García-Lorenzo B., Mediavilla E., 2006b, in Arribas S., Mediavilla E., Roth M., eds, Proceedings of the XIII IAC Winter School, in press

Sérsic J. L., 1968, Atlas de Galaxias Australes. Press of the Universidad Nacional, Córdoba, Argentina

Simien F., de Vaucouleurs G., 1986, ApJ, 302, 564

Sirianni M. et al., 2005, PASP, 117, 1049

Smail I., Dressler A., Couch W. J., Ellis R. S., Oemler A. J., Butcher H., Sharples R. M., 1997, ApJS, 110, 213

Smail I., Edge A. C., Ellis R. S., Blandford R. D., 1998, MNRAS, 293, 124

Smail I., Knutschner H., Kodama T., Smith G. P., Packham C., Fruchter A. S., Hook R. N., 2001, MNRAS, 323, 839

Stanford S. A., Elston R., Eisenhardt P. R., Spinrad H., Stern D., Dey A., 1997, AJ, 114, 2232

Stanford S. A., Eisenhardt P. R., Dickinson M., 1998, ApJ, 492, 461

Thomas D., Greggio L., Bender R., 1999, MNRAS, 302, 537

Thomas D., Maraston C., Korn A., 2004, MNRAS, 351, L19

Thompson L. A., 1986, ApJ, 300, 639

Thompson L. A., 1988, ApJ, 324, 112

Thuan T. X., Gunn J. E., 1976, PASP, 88, 543

Tinsley B., 1980, Fund. Cosm. Phys., 5, 287

Tody D., 1993, in Hanisch R. J., Brissenden R. J. V., Barnes J., eds, ASP Conf. Ser. Vol. 52, IRAF in the Nineties in Astronomical Data Analysis Software and Systems II. Astron. Soc. Pac., San Francisco, p. 173

Trager S. C., Worthey G., Faber S. M., Burstein D., Gonzalez J. J., 1998, ApJS, 116, 1

Trager S. C., Faber S. M., Worthey G., Gonzalez J. J., 2000, AJ, 120, 165

Vazdekis A., Cenarro A. J., Gorgas J., Cardiel N., Peletier R. F., 2003, MNRAS, 340, 1317

van Dokkum P. G., Franx M., 1996, MNRAS, 281, 985

van Dokkum P. G., Franx M., 2001, ApJ, 553, 90

Verheijen M. A. W., 1997, PhD thesis, Univ. Groningen

Verheijen M. A. W., Bershady M. A., Andersen D. R., Swaters R. A., Westfall K., Kelz A., Roth M. M., 2004, Astron. Nachr., 325, 151

Wolf C. et al., 2005, ApJ, 630, 771

Worthey G., 1994a, ApJS, 95, 107

Worthey G., 1994b, ApJS, 111, 377

Worthey G., Faber S. M., González J. J., Burstein D., 1994, ApJS, 94, 687

Ziegler B. L., Bower R. G., Smail I., Davies R. L., Lee D., 2001, MNRAS, 325, 1571

Zwaan M. A., van Dokkum P. G., Verheijen M. A. W., 2001, Sci, 293, 1800

APPENDIX A: INDIVIDUAL SPECTRUM

Fig. A1 shows the individual spectrum extracted from our IFS data for each galaxies listed in Table 4. For each galaxy the
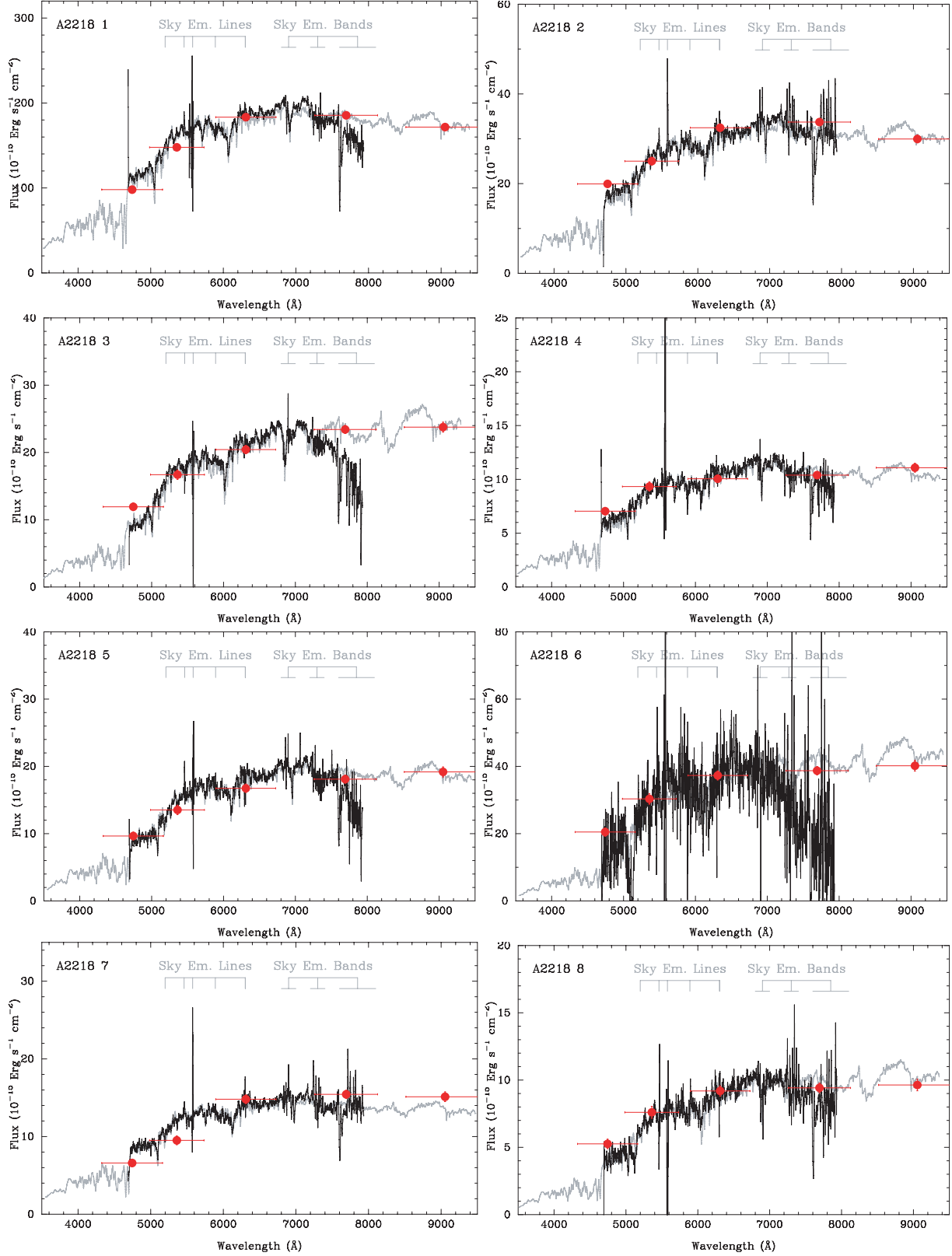
Figure A1. Individual extracted spectrum for each of the confirmed cluster members within the field of view of our IFS data (black solid line), each one labelled with the identification number listed in Table 4. For each galaxy the spectrum is plot together with the multiband broad-band photometry derived from the *HST*/ACS F475W-, F555W-, F625W-, F775W- and F850LP-band images (red circles). The vertical error bars indicate the photometric errors, while the horizontal ones indicate the width of each band. The grey solid line shows the best-fitting SSP model derived with the procedure described in Section 3.7.2.
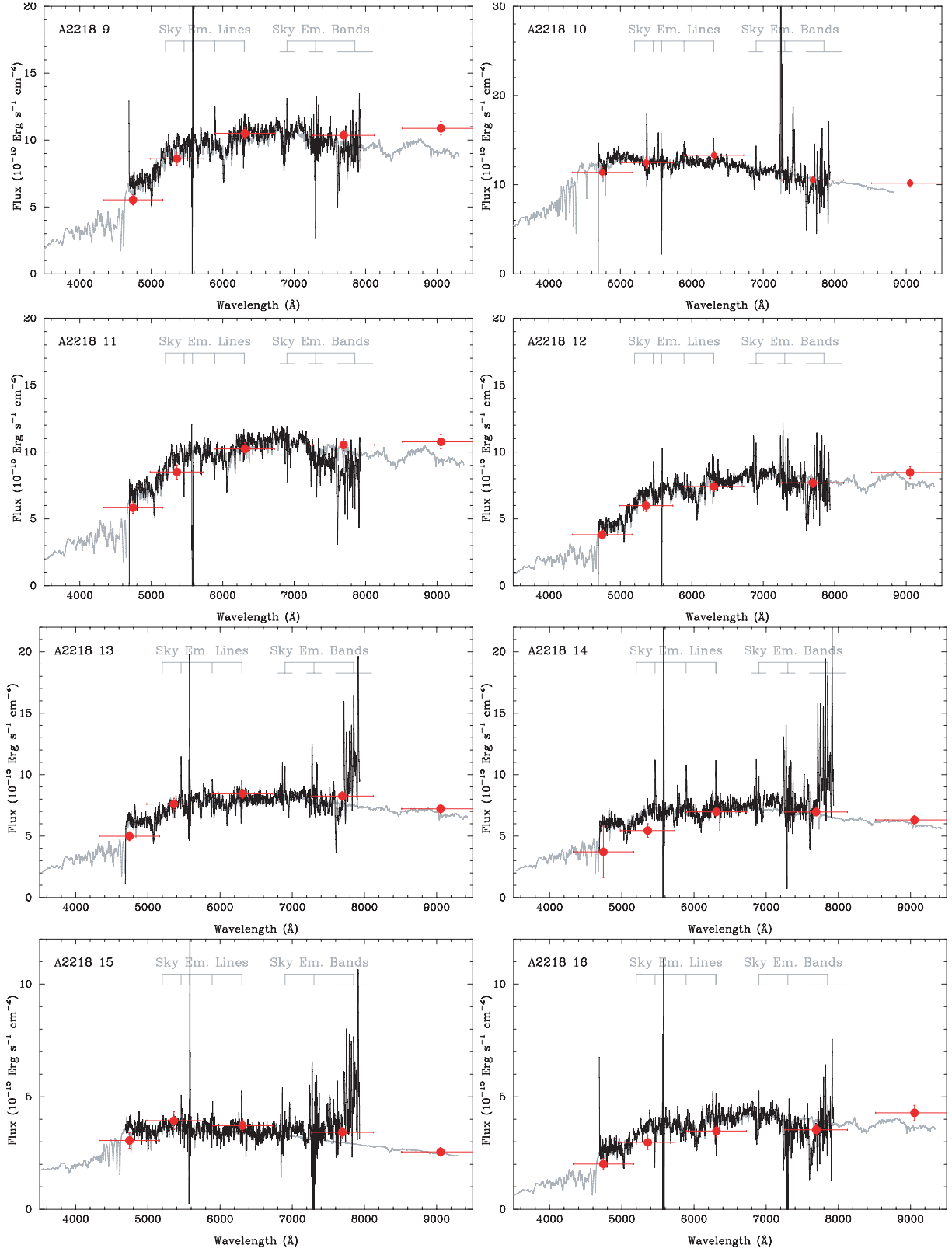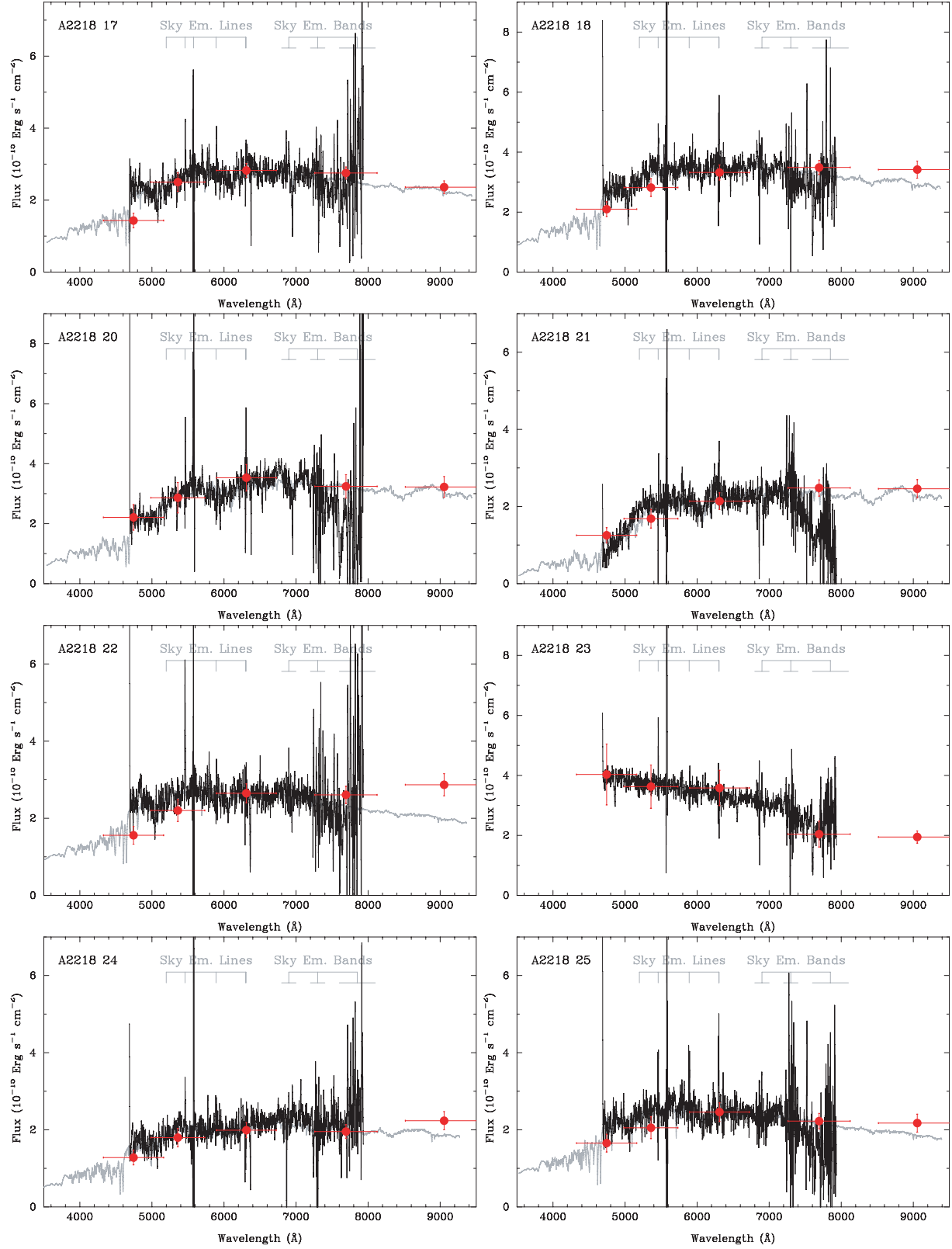
Figure A1 – *continued*
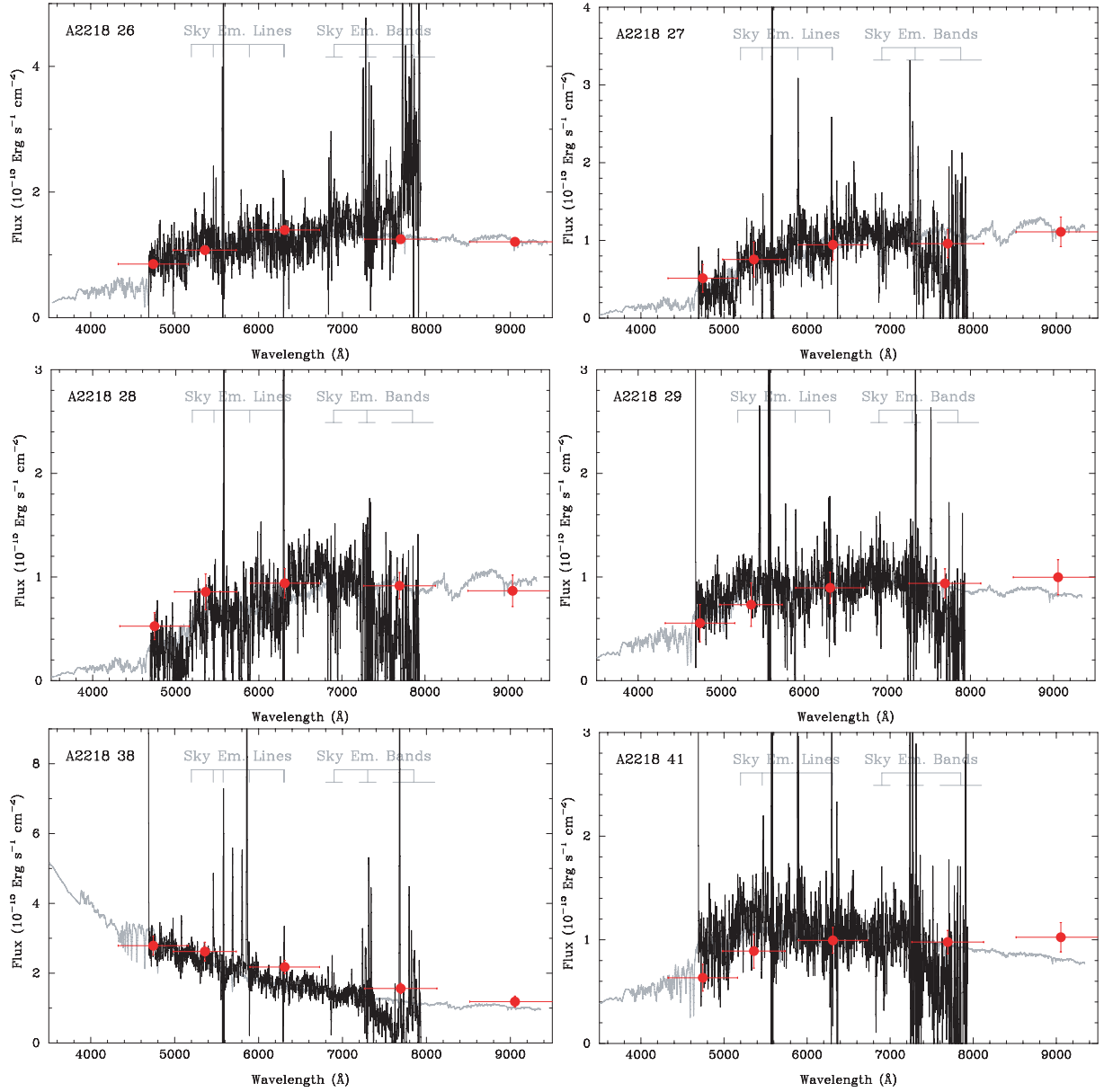
Figure A1 – *continued*

Figure A1 – *continued*

spectrum is plot together with the multiband broad-band photometry derived from the *HST*/ACS F475W-, F555W-, F625W-, F775W- and F850LP-band images (red circles). The vertical error bars indicate the photometric errors, while the horizontal ones indicate the width of each band. The wavelength of the strongest night-sky emission lines and bands are also indicated. At these locations the improper sky subtraction produces characteristic residuals that can be seen in the spectra. In particular the wavelength range redder than 7200 Å is strongly affected, so we did not consider it in any of the performed analysis. The grey solid line shows the best-fitting SSP model derived with the procedure described in Section 3.7.2.

APPENDIX B: MORPHOLOGICAL ANALYSIS AND SPECTRA EXTRACTION: CHROMATIC EFFECTS

The procedure to deblend and extract the spectra of the individual objects from our IFS data relies on the assumption that it is possible to use the morphological parameters derived by fitting galaxy profile models on the F850LP-band image, using GALFIT, to derive the photometry at any other wavelength range, by forcing GALFIT to recover the flux with the morphological parameters fixed. To test this assumption use the *HST*/ACS multiband image data set, which cover all the wavelength range or our IFS data.

For each broad-band image of our data set (F475W, F555W, F625W and F775W), we performed the same morphological analysis that we already performed for the F850LP band, following the prescriptions described in Section 3.2. In this first iteration we left GALFIT to fit the morphological parameters, as we did in the analysis of the F850LP band. This procedure produces a morphological catalogue for each of the considered images, including the same parameters listed in Table 3. In a second iteration, the analysis was repeated but this time we used as input parameters the ones derived by the analysis of the F850LP-band image. In this second step the morphological parameters were fixed to those input values, and only the photometry was fitted by GALFIT. This procedure is basically the same that we use to extract and deblend the spectra in our IFS data.

Similar results have been found for any band. Fig. B1 summarizes the results from the analysis. Left-hand panel shows a comparison between the different bands magnitudes derived by GALFIT forcing the morphological parameters to be the ones derived from the morphological analysis of the F850LP-band image, and the magnitudes derived not imposing any condition to GALFIT regarding the morphological parameters of the analysed objects. The magnitudes derived using both methods agree within ± 0.2 mag, without any clear trend or bias. Middle panel shows the scalelength derived by GALFIT for the F850LP-band image, using in the forced fitting process over the different bands' images described above, along the scalelength derived directly over this image by the morphological analysis. Although there are some outlayers, both scalelengths are similar in most of the cases. Right-hand panels shows a similar comparison between the Sérsic indices derived by the two fitting procedures. In this last case we found the biggest differences between both parameters, with a considerable dispersion from the one-to-one relation. It is clear that there is a chromatic effect over the morphology, as it is seen in the last panel, however, this effect has a reduced impact on the derived scalelength, and even less impact on the derived photometry. Thus, the basic assumption of our procedure to deblend and extract the individual spectra of the targets from our IFS data is valid.

To perform a final test of the validity of our procedure and the accuracy of our spectrophotometric data we synthesized the fluxes throughout the *B*, *V*, *R* and *I* bands for each of our 28 cluster members with IFS data by convolving their extracted spectra with the corresponding *HST*/ACS filter band transmission curve, integrating their fluxes. These fluxes are compared to the corresponding ones derived using the *HST*/ACS based photometry listed in Table 2. Fig. B2 shows the histograms of the relative differences between both fluxes for each band, $\Delta F/F$, that basically corresponds to the error in the corresponding magnitude ($\sim e_{mag}$). Due to the high accuracy of the *HST*/ACS photometry (typical $e_{mag} \sim 0.05$ mag for the considered objects) most of the differences shown in the figure corresponds to spectrophotometric errors in the IFS data. For all the bands both fluxes agree within a range of ± 0.3 mag, with an s.d. of the difference of ~ 0.15 mag.
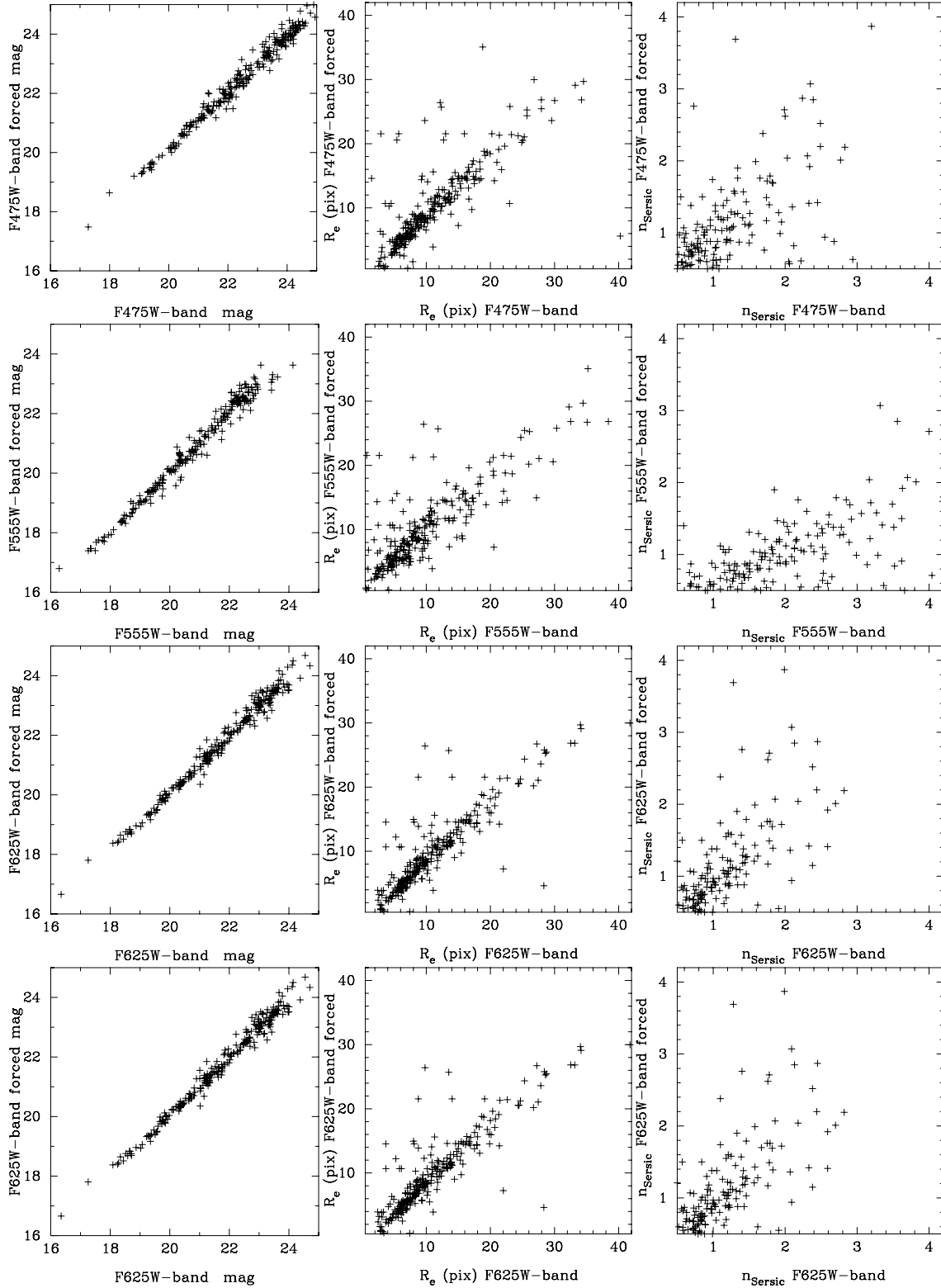
Figure B1. Left-hand panels: F475W-, F555W-, F625W- and F775W-band magnitudes derived by GALFIT forcing the morphological parameters to be the ones derived from the morphological analysis of the F850LP-band image, as a function of the same magnitudes derived not imposing any condition to GALFIT regarding the morphological parameters of the analysed objects. Middle panels: similar comparison for the length-scales derived by GALFIT for the F850LP-band image and for any other band. Right-hand panels: similar comparison for the Sérsic indices.
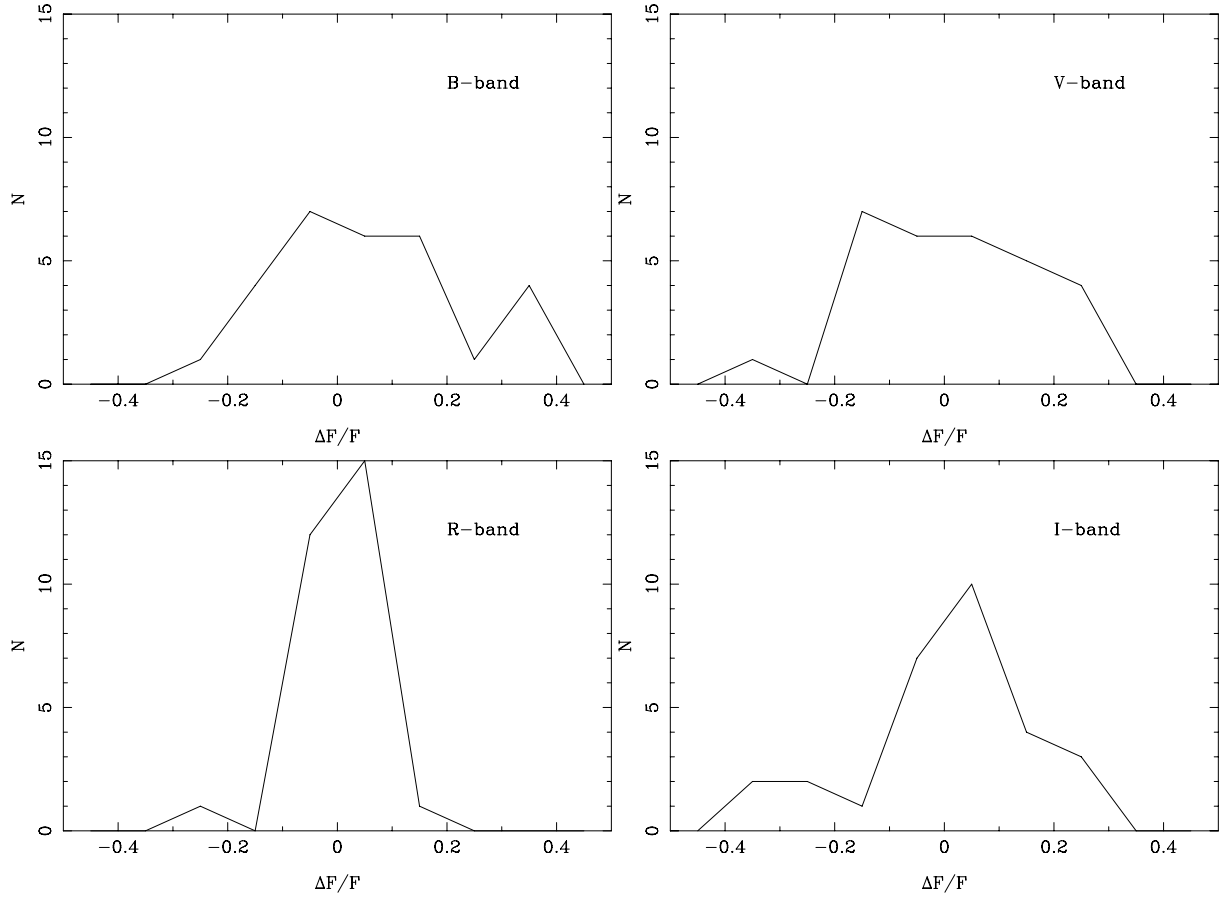
Figure B2. Relative differences between the fluxes obtained for the *B*, *V*, *R* and *I* bands derived from the IFS extracted spectra and those ones derived using the photometry obtained from the *HST*/ACS images.

This paper has been typeset from a TEX/LATEX file prepared by the author.